Quasi-two-dimensional liquid-metal magnetohydrodynamics and the anticipated vorticity method

By P A U L J. D E L L A R†

OCIAM, Mathematical Institute, 24–29 St Giles', Oxford, OX1 3LB, UK

The flow of liquid metal in a magnetic field may become almost two-dimensional because the magnetic field inhibits velocity variations along the field lines. Two-dimensionality must break down near rigid boundaries to satisfy no-slip boundary conditions, leading to a quasi-two-dimensional flow comprising a two-dimensional core between Hartmann boundary layers. Flow in the Hartmann layers is dominated by viscosity and the Lorentz force. Pothérat, Sommeria & Moreau (*J. Fluid Mech.* vol. 424, 2000, p. 75, referred to herein as PSM) recently proposed a two-dimensional equation for the vertically averaged horizontal velocity to describe such flows. Their treatment extends previous work to account for inertial corrections (such as Ekman pumping) to the flow in the Hartmann layers. The inertial corrections lead to extra nonlinear terms in the vertically averaged equations, including terms with mixed spatio-temporal derivatives, in addition to the algebraic drag term found previously. The present paper shows that many of these terms coincide with a previously postulated model of two-dimensional turbulence, the anticipated vorticity method, and a subsequent modification restoring linear and angular momentum conservation that might be described as an anticipated velocity method. A fully explicit version of PSM's equation is derived, with the same formal accuracy but no spatio-temporal derivatives. This explicit equation is shown to dissipate energy, although enstrophy may increase. Numerical experiments are used to compare the effect of the various different equations (without linear drag or forcing) on both laminar and turbulent initial conditions. The mixed spatio-temporal derivatives in PSM's original equation lead to a system of differential-algebraic equations, instead of ordinary differential equations, after discretizing the spatial variables. Such systems may still be solved readily using existing software. The original and explicit versions of PSM's equation give very similar results for parameter regimes representative of laboratory experiments, and give qualitatively similar results to the anticipated velocity method. The anisotropic diffusion of vorticity along streamlines that is present in all equations studied except the Navier–Stokes equations has comparatively little effect. The additional terms in PSM's equation, and also the anticipated velocity method, that arise from Ekman pumping are much more significant. These terms lead to an outward transport of vorticity from coherent vortices, so solutions of equations with these extra terms appear much more organized and have less fine-scale structure than solutions of the Navier–Stokes equations, or even the anticipated vorticity method, with the same initial conditions. This has implications for the extent to which the self-organizing behaviour and appearance of global modes seen in laboratory experiments

† Present address: Department of Mathematics, Imperial College London, London, SW7 2AZ, UK; paul.dellar@na-net.ornl.gov

with thin liquid-metal layers and magnetic fields may be attributed to self-organizing properties of the unmodified two-dimensional Navier–Stokes equations.

1. Introduction

Perhaps the original motivation for studying the two-dimensional Navier–Stokes equations and two-dimensional turbulence (Kraichnan & Montgomery 1980; Frisch 1995; Tabeling 2002) is as a model for the large-scale behaviour of the atmosphere and oceans. Although the latter are more correctly described by geostrophic turbulence, the qualitative behaviour is very similar (Rhines 1979; Salmon 1998). Another motivation is as an interesting application of statistical mechanics (Kraichnan 1967; Rhines 1979; Robert & Sommeria 1991; Miller, Weichman & Cross 1992; Tabeling 2002). Originally studied only theoretically and computationally, two-dimensional turbulence has since been realized experimentally in soap films (as reviewed by Kellay & Goldburg 2002), in liquid metals permeated by magnetic fields (as reviewed by Moreau 1998, 1990), and also in non-neutral plasmas.

Meanwhile, various equations resembling the two-dimensional Navier–Stokes equations have been derived to describe thin fluid layers, with either free surfaces or rigid lids, by averaging the relevant three-dimensional equations across the layer (e.g. Green & Naghdi 1976; Miles & Salmon 1985; Camassa, Holm & Levermore 1996; Dellar 2003). The purpose of this paper is to compare the layer-averaged equation obtained by Pothérat, Sommeria & Moreau (2000, hereafter referred to as PSM), to describe a thin layer of liquid metal in a perpendicular magnetic field, with a model for two-dimensional turbulence called the anticipated vorticity method (AVM) devised by Sadourny & Basdevant (1981, 1985, see also Basdevant & Sadourny 1983), and its extension to the 'anticipated velocity method' by Benzi, Succi & Vergassola (1990, 1992, see also Dellar 2004).

Magnetic fields may be used to simulate two-dimensional turbulence in electrically conducting fluids because the Lorentz force has the effect of suppressing velocity variations in the direction of the magnetic field. In the parameter regime typical for liquid metals on laboratory scales this suppression takes the form of degenerate Alfvén waves propagating along the field lines to eliminate velocity variations (see § 2). The flow therefore tends to become approximately two-dimensional, and independent of the coordinate aligned with the magnetic field (Roberts 1967; Alemany *et al.* 1979; Sommeria & Moreau 1982; Davidson 1995, 2001).

Kolesnikov & Tsinober (1974) made some of the first experimental measurements showing suppression of three-dimensional turbulence by a magnetic field. They used a mercury analogue of a wind tunnel, a rectangular duct $50 \, \text{mm} \times 60 \, \text{mm}$ in cross-section through which mercury flowed at about $0.2 \, \text{m s}^{-1}$. A grid at the inlet generated three-dimensional turbulence. By inferring velocity fluctuations from electrodes at the walls, they saw a transition from the $k^{-5/3}$ energy spectrum characteristic of three-dimensional turbulence with the device in a weak $0.08 \, \text{T}$ magnetic field, to a k^{-3} energy spectrum characteristic of two-dimensional turbulence when they applied a stronger $0.8 \, \text{T}$ magnetic field. This transition to an apparently two-dimensional flow was supported by measurements of the two different flows' transport properties using a passive tracer (indium) injected at one point just behind the grid, and sampled downstream through a line of narrow tubes across the duct.

However, Alemany *et al.* (1979) later conducted similar experiments in a larger cylindrical vessel, 0.2 m in internal diameter and 2.7 m high, filled with mercury and placed in a magnetic field of up to 0.2 T. Grid turbulence was generated by a moving grid driven through the mercury at up to 0.8 m s^{-1}. They observed transitions from $k^{-5/3}$ to k^{-3} energy spectra even for almost isotropic flows that were far from two-dimensional. They attributed this change in the energy spectrum to Joule dissipation extracting energy at all scales, modifying Kolmogorov's hypothesis (leading to a $k^{-5/3}$ spectrum) that dissipation is negligible in the inertial range and acts only at very high wavenumbers. Their modified version of Kolmogorov's argument leads to a k^{-3} energy spectrum even for three-dimensional flows. For further discussion see Sommeria & Moreau (1982).

A second series of experiments begun by Sommeria (1986, 1988) used a closed domain, 12 cm square in the horizontal plane, containing a 2 cm deep layer of mercury with a vertical magnetic field to enforce two-dimensionality. Instead of pumping mercury through the device as above, these flows are forced electromagnetically by injecting current through electrodes at the lower boundary. The electrodes have the effect of imposing a divergence-free horizontal body force in the vertically averaged flow (see equation (2.4) below), although they do also drive three dimensional behaviour in small regions around the electrodes (Sommeria 1988). This device was used initially by Sommeria (1986) to study the inverse energy cascade in two-dimensional turbulence, by forcing the flow at small lengthscales through a regular array of 36 electrodes in the lower boundary. Sommeria observed a $k^{-5/3}$ energy spectrum when the experimental parameters were such that boundary friction limited the inverse cascade. For smaller effective frictions the inverse cascade extended to fill the domain, resulting in a globally rotating coherent mode of the kind predicted by Kraichnan (1967). Sommeria (1988) subsequently used the same device to study the behaviour of axisymmetric vortices driven by current injected at a single electrode. A more recent series of experiments in a circular domain has used currents injected through a ring made up of many closely spaced electrodes to drive an axisymmetric shear flow, that in turns develops into a turbulent shear layer through Kelvin–Helmholtz instabilities (Moreau 1998; Alboussière, Uspenski & Moreau 1999; Messadek & Moreau 2002). These experiments take place in a much stronger magnetic field of up to 6 T, compared with the 1 T maximum in Sommeria's earlier experiments.

The quasi-two-dimensionality enforced by the magnetic field in these experiments must break down near rigid boundaries in order to satisfy no-slip boundary conditions. For typical laboratory-scale liquid metal magnetohydrodynamics (MHD), this transition takes place within thin boundary layers called Hartmann layers of width $O(Ha^{-1})$, where the Hartmann number $Ha = B_0 a / \sqrt{\rho \eta_* \nu_*} \gg 1$, giving rise to a flow profile as sketched in figure 1. Here a is the layer depth, B_0 the imposed field strength, and ρ the density. The fluid's kinematic viscosity is ν_*, and its magnetic diffusivity is η_*. An asterisk denotes dimensional values for these diffusivities. For mercury in a 1 T magnetic field the dimensional width a/Ha of the Hartmann layer is about 40 µm, whereas the layer depth is perhaps a centimetre in laboratory experiments. The region between the two Hartmann layers where the velocity $\boldsymbol{u} \approx \boldsymbol{u}_c(x, y)$ is approximately horizontal and independent of z is called the core. This flow configuration develops from impulsively started motion in a fluid with finite viscosity and resistivity through Alfvén waves propagating away from the boundaries, leaving Hartmann layers behind (Shercliff 1965, pp. 160–166; Moreau 1990, pp. 165–171).

The Hartmann layers are dominated by a balance between viscous and Lorentz forces. Since the Lorentz force is linear at low magnetic Reynolds numbers, to a
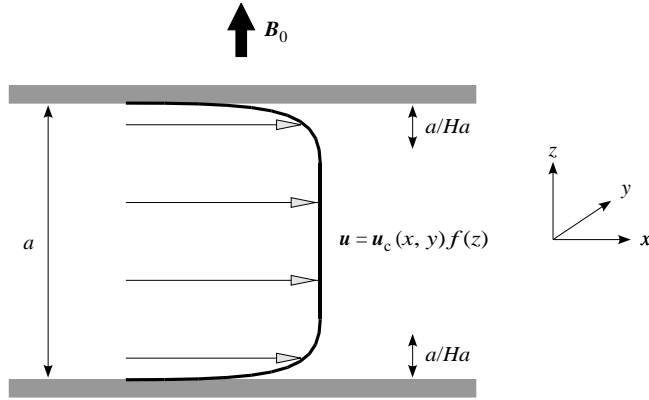
FIGURE 1. Hartmann layers form on walls perpendicular to the imposed magnetic field $\boldsymbol{B}_0$. The core velocity $\boldsymbol{u}_c$ decays to zero over a distance $a/Ha = \sqrt{\rho\eta_* \nu}/B_0$ to satisfy the no-slip boundary condition on the walls.

first approximation the Hartmann layers respond linearly to the core flow. This led Sommeria & Moreau (1982) to derive two-dimensional equations for the vertically averaged horizontal velocity that included a linear friction term due to the Hartmann layers occurring on rigid surfaces perpendicular to the imposed magnetic field (see also Frank, Barleon & Muller 2001; Bühler 1996):

$$\partial_t \overline{\boldsymbol{u}} + \overline{\boldsymbol{u}} \cdot \nabla \overline{\boldsymbol{u}} + \nabla \overline{p} = \nu_* \nabla^2 \overline{\boldsymbol{u}} + \frac{1}{t_{\mathrm{H}}}(\overline{\boldsymbol{u}}_0 - n\overline{\boldsymbol{u}}), \tag{1.1}$$

where $t_{\mathrm{H}} = a^2/(\nu_* Ha)$ is the Hartmann braking time, and an overbar denotes a vertical average across the layer. Also, n denotes the number of Hartmann layers, so $n = 2$ for a flow confined between two rigid walls as in figure 1, while $n = 1$ for a flow with an upper free surface. Since mercury rapidly forms a rigid oxide coating when exposed to air, genuine free surface flows only arise for experiments conducted in inert gases (Sommeria 1986). The linear algebraic drag term $-\overline{\boldsymbol{u}}/t_{\mathrm{H}}$ represents the leading-order effect of the Hartmann boundary layers on the core flow. Exactly the same kind of effective equation arises in Hele-Shaw flow of viscous fluid between two parallel closely spaced plates, though in Hele-Shaw flow the velocity profile across the layer is parabolic, like Poiseuille flow, rather than the two exponential boundary layers with a uniform core sketched in figure 1. The driving velocity $\overline{\boldsymbol{u}}_0$ in (1.1) arises from current injection at the boundaries (see §2) and vanishes for electrically insulating boundaries. A linear drag appears under the name of 'Rayleigh friction' in many approximate models arising in geophysical fluid dynamics (Salmon 1998), a comparison made previously by Sommeria (1986), while a driving term like $\overline{\boldsymbol{u}}_0/t_{\mathrm{H}}$ appears as the 'Neptune effect' in some ocean models for flow over varying topography (Holloway 1992).

Equation (1.1) is formally valid in the limit when the Hartmann number Ha and a second dimensionless quantity $N = B_0^2 a/(\rho\eta_* U)$ are both large. This second quantity is usually called the interaction parameter, and estimates the ratio of the Lorentz force to inertia. By contrast, the square of the Hartmann number estimates the ratio of Lorentz to viscous forces. The two parameters are thus related by

$$Re_{\parallel} N = Ha^2, \tag{1.2}$$

where $Re_\parallel = Ua/\nu_*$ is the usual fluid Reynolds number based on the layer depth a, the lengthscale parallel to the magnetic field. To give some idea of the orders of magnitude that arise in the laboratory experiments described above, consider a layer of mercury 10 cm wide and 1 cm deep, flowing at $10\,\mathrm{cm\,s^{-1}}$ in a 1 T magnetic field. The relevant parameters are then

$$Ha = 260, \quad N = 7.8, \quad \delta = 0.1, \quad t_\mathrm{H} = 3.3 \text{ s}, \quad \nu_* = 10^{-7}\mathrm{m^2\,s^{-1}}, \qquad (1.3)$$

where δ is the aspect ratio. While $Ha \gg 1$ seems amply satisfied, the assumption that $N \gg 1$, or that inertia is weak, is rather more questionable. In fact Sommeria (1988) attributed the spreading of his axisymmetric vortices beyond the amount predicted by the model (1.1) to inertially driven recirculation (Ekman pumping) in the Hartmann layers.

For this reason PSM recently derived a more complicated model that extends the previous equation (1.1) to include the leading-order inertial correction to the dominant Lorentz–viscous force balance in the Hartmann layers. By vertically averaging these inertial corrections they obtained the equation

$$\partial_t \overline{\boldsymbol{u}} + \overline{\boldsymbol{u}} \cdot \nabla \overline{\boldsymbol{u}} + \nabla \overline{p} = \nu_* \nabla^2 \overline{\boldsymbol{u}} + \frac{1}{t_\mathrm{H}}(\overline{\boldsymbol{u}}_0 - n\alpha\overline{\boldsymbol{u}}) + \frac{nt_\mathrm{H}}{Ha^2}\left(\tfrac{7}{36}\mathscr{D}_{\overline{\boldsymbol{u}}} + \tfrac{1}{8}\partial_t\right)\overline{\boldsymbol{u}} \cdot \nabla \overline{\boldsymbol{u}}, \qquad (1.4)$$

where $\alpha = 1 + n/Ha$, and the linear operator $\mathscr{D}_{\overline{\boldsymbol{u}}}$ is defined by

$$\mathscr{D}_{\overline{\boldsymbol{u}}}\boldsymbol{F} = \overline{\boldsymbol{u}} \cdot \nabla \boldsymbol{F} + \boldsymbol{F} \cdot \nabla \overline{\boldsymbol{u}}. \qquad (1.5)$$

For future convenience we introduce a dimensionless version of (1.4),

$$\partial_t \boldsymbol{u} + \boldsymbol{u} \cdot \nabla \boldsymbol{u} + \nabla p = \nu \nabla^2 \boldsymbol{u} + \kappa(\boldsymbol{u}_0 - \boldsymbol{u}) + \beta\left(\tfrac{7}{36}\mathscr{D}_{\boldsymbol{u}} + \tfrac{1}{8}\partial_t\right)\boldsymbol{u} \cdot \nabla \boldsymbol{u}, \qquad (1.6)$$

and suppress the overbars on $\overline{\boldsymbol{u}}$ and $\overline{p}$ in the dimensionless equation. The parameter $\nu = \nu_*\delta/(Ua)$ is a dimensionless viscosity, equal to the reciprocal of the Reynolds number based on a horizontal lengthscale a/δ. Since the kinematic viscosity ν_* for mercury is about ten times smaller than for water, even 10 cm sized laboratory experiments may attain high fluid Reynolds numbers.

We absorb the factor of $n\alpha$ in front of $\boldsymbol{u}$ in (1.4) into the dimensionless drag coefficient $\kappa = (1 + n\alpha)t_\mathrm{e}/t_\mathrm{H}$ to simplify later calculations, and redefine $\boldsymbol{u}_0$ by a factor of $(1+n\alpha)^{-1}$ to compensate. The dominant part $t_\mathrm{e}/t_\mathrm{H}$ of the drag coefficient is the ratio of a horizontal eddy turnover time $t_\mathrm{e} = a/(\delta U)$ to the Hartmann braking time t_H. The reciprocal quantity $t_\mathrm{H}/t_\mathrm{e}$ was denoted R_h by Sommeria (1986), although Sommeria considered a forced–dissipative system (see §2 below) in which the velocity scale U was set by balancing the forcing from current injection against Hartmann braking, instead of being set by the initial conditions. The final parameter $\beta = n\delta/(NHa)$ combining the Hartmann and interaction parameters measures the significance of inertia in the Hartmann layers. Assuming rigid upper and lower boundaries ($n = 2$) and parameter values from (1.3) above, the combinations appearing in (1.6) are

$$\nu = \frac{\delta N}{Ha^2} = 10^{-5}, \quad \beta = \frac{n\delta}{NHa} = 10^{-4}, \quad \kappa = \frac{t_\mathrm{e}}{t_\mathrm{H}}\left(1 + \frac{n}{Ha}\right) = \frac{N}{\delta Ha}\left(1 + \frac{n}{Ha}\right) = 0.3. \tag{1.7}$$

As n and the aspect ratio δ are fixed by the geometry of an experiment, the three parameters ν, β, and κ cannot be varied independently. The two independent control parameters are Ha and N, which depend on the applied magnetic field and injected current.

Since $\nabla \cdot \boldsymbol{u} = 0$, we may introduce a streamfunction ψ such that $\boldsymbol{u} = (-\psi_y, \psi_x, 0)$. The vorticity vector is then $\boldsymbol{\omega} = \nabla \times \boldsymbol{u} = (0, 0, \omega)$, where $\omega = +\nabla^2 \psi$ is the only non-zero component. The choice of a $+$ sign in the relation between ω and ψ is the usual convention in both MHD (e.g. Verron & Sommeria 1987) and geophysical fluid dynamics (e.g. Salmon 1998). PSM's equation (1.6) thus becomes

$$\partial_t \omega + [\psi, \omega] = \nu \nabla^2 \omega + \kappa(\omega_0 - \omega) + \tfrac{1}{8}\beta \partial_t [\psi, \omega]$$

$$+ \tfrac{7}{36}\beta\{[\psi, [\psi, \omega]] + [\psi_y, \omega\psi_x] + [\omega\psi_y, \psi_x]\}, \quad (1.8)$$

where $[f, g] = f_x g_y - f_y g_x$ denotes the Jacobian of two functions, so that $[\psi, \omega] = \boldsymbol{u} \cdot \nabla \omega$, and $\omega_0 = \hat{\boldsymbol{z}} \cdot \nabla \times \boldsymbol{u}_0$.

The purpose of this paper is to investigate the effects of the additional terms in (1.4) and (1.6) compared with the earlier model (1.1). In particular, we compare the properties of these extra terms with the terms appearing in the anticipated vorticity method (AVM) previously devised by Sadourny & Basdevant (1981, 1985, see also Basdevant & Sadourny 1983), and its extension to what might be called the 'anticipated velocity method' by Benzi *et al.* (1990, 1992, see also Dellar 2004). The anticipated vorticity method postulates the replacement

$$\partial_t \omega + \boldsymbol{u} \cdot \nabla(\omega - \lambda \boldsymbol{u} \cdot \nabla \omega) = 0, \quad (1.9)$$

for the usual two-dimensional inviscid vorticity equation $\partial_t \omega + \boldsymbol{u} \cdot \nabla \omega = 0$. It is intended to model two-dimensional turbulence at high Reynolds numbers, i.e. small viscosities ν. The extra term proportional to the positive parameter λ has various properties, like conserving energy while monotonically dissipating enstrophy (see §3) and preserving steady states, that make it attractive for modelling two-dimensional turbulence, which is characterized by a much more rapid selective decay of enstrophy than energy. In numerical experiments, Vallis & Hua (1988) found that the AVM performed as well or better than a conventional eddy viscosity parametrization, and was competitive with other turbulence models of similar complexity.

Equation (1.9) may be rewritten as $\partial_t \omega + \boldsymbol{u} \cdot \nabla \omega = \lambda \nabla \cdot (\boldsymbol{u}\boldsymbol{u} \cdot \nabla \omega)$ which corresponds to a well-posed but degenerate (and anisotropic) parabolic equation with diffusivity tensor $\lambda \boldsymbol{u}\boldsymbol{u}$ that only diffuses vorticity along streamlines (see §3). This anisotropic diffusion of vorticity causes enstrophy to decay, and energy to be conserved. The name 'anticipated vorticity' arises because $\omega - \lambda \boldsymbol{u} \cdot \nabla \omega$ in equation (1.9) approximates the vorticity ω at a later time $t + \lambda$ when λ is small (Sadourny & Basdevant 1981; Vallis & Hua 1988). Thus equation (1.9) resembles a numerical predictor–corrector timestepping scheme, in which the expression $-\boldsymbol{u} \cdot \nabla \omega$ for $\partial_t \omega$ is evaluated at the end of a timestep of length λ. After restoring the usual viscous term, equation (1.9) may also be rewritten as

$$\partial_t \omega + [\psi, \omega] = \nu \nabla^2 \omega + \lambda [\psi, [\psi, \omega]], \quad (1.10)$$

where the extra $\lambda [\psi, [\psi, \omega]]$ term coincides with the first term inside the braces $\{\cdot\}$ in equation (1.8).

The anticipated vorticity method bears some resemblance to the Leray turbulence models (Leray 1934, see also Geurts & Holm 2003),

$$\partial_t \boldsymbol{u} + \langle \boldsymbol{u} \rangle \cdot \nabla \boldsymbol{u} + \nabla p = \nu \nabla^2 \boldsymbol{u}, \quad (1.11)$$

where $\langle \boldsymbol{u} \rangle$ is some smoothed version of $\boldsymbol{u}$, for instance the result of applying a Gaussian filter to $\boldsymbol{u}$. The quantity $\omega - \lambda \boldsymbol{u} \cdot \nabla \omega$ in equation (1.9) is intended to model the unsmoothed combination $\overline{\omega} + \omega'$ appearing in the derivation (see §3), so the

anticipated vorticity method also advects with a smoother velocity field than the advected quantity. In particular, it shares the shortcoming of the Leray model that the associated momentum equation for $\boldsymbol{u}$ cannot be written as the divergence of a symmetric stress tensor, and so cannot be readily expressed in kinetic theory terms (see §4). This led Benzi *et al.* (1990, 1992) to propose the alternative

$$\partial_t \boldsymbol{u} + \nabla \cdot \{\boldsymbol{uu} + p\boldsymbol{I} - \lambda \left(\boldsymbol{u}(\boldsymbol{u} \cdot \nabla \boldsymbol{u}) + (\boldsymbol{u} \cdot \nabla \boldsymbol{u})\boldsymbol{u}\right)\} = 0, \tag{1.12}$$

which may also be written as

$$\partial_t \boldsymbol{u} + \boldsymbol{u} \cdot \nabla \boldsymbol{u} + \nabla p = \lambda \{\mathscr{D}_{\boldsymbol{u}}(\boldsymbol{u} \cdot \nabla \boldsymbol{u}) + \boldsymbol{u} \nabla \cdot (\boldsymbol{u} \cdot \nabla \boldsymbol{u})\}. \tag{1.13}$$

The $\mathscr{D}_{\boldsymbol{u}}(\boldsymbol{u} \cdot \nabla \boldsymbol{u})$ term is identical to that in equation (1.6). Although the other additional terms differ, the qualitative behaviour of the two equations (1.6) and (1.13) is shown below to be quite similar. In streamfunction–vorticity form, equation (1.13) with an additional Newtonian viscous term becomes

$$\partial_t \omega + [\psi, \omega] = \nu \nabla^2 \omega + \lambda \{[\psi, [\psi, \omega]] + [\psi_y, \omega \psi_x] + [\omega \psi_y, \psi_x] + 2\nabla \cdot ([\psi_y, \psi_x] \nabla \psi)\}, \tag{1.14}$$

using the formulae $\nabla \cdot (\boldsymbol{u} \cdot \nabla \boldsymbol{u}) = 2[\psi_y, \psi_x]$, and $\hat{\boldsymbol{z}} \cdot \nabla \times (F\boldsymbol{u}) = \nabla \cdot (F \nabla \psi)$ for any $F(x, y, t)$. The first three terms inside the braces $\{\cdot\}$ in equation (1.14), arising from $\nabla \times \mathscr{D}_{\boldsymbol{u}}(\boldsymbol{u} \cdot \nabla \boldsymbol{u})$, coincide with the terms inside the braces $\{\cdot\}$ in equation (1.8).

In the subsequent sections we first outline the derivations of the PSM and AVM equations, compare their properties in more detail, and study their effect on linear vorticity waves. Using numerical experiments, we compare the effects of these models, and some alternative versions, on a deterministic two-dimensional flow exhibiting the rolling up of shear layers, and the evolution of two-dimensional turbulence from random initial conditions. The PSM equation is implicit in time, like the Green–Naghdi (1976) and dispersive shallow water MHD (Dellar 2003) equations that also arise from layer-averaging, due to the $\partial_t [\psi, \omega]$ term on the right-hand side of equation (1.8). This property poses no great obstacle to numerical solution, because the finite system of equations obtained by discretizing the spatial dependence of ω using Fourier series is readily formulated and solved as a system of differential-algebraic equations (DAEs) rather than ordinary differential equations.

The linear drag and forcing terms in the PSM equation are very prominent in laboratory parameter regimes, as shown by the value $t_e/t_H \approx 0.3$ estimated above. In other words, the Hartmann braking time is only three eddy turnover times, at least for large eddies that fill the domain. This is partly because strong magnetic fields are desirable to enhance the two-dimensionality of the core flow, but strong fields simultaneously increase the drag from the Hartmann layers. For this reason the shallow-layer laboratory experiments described above are all forced-dissipative systems that rely upon substantial driving from injected currents to overcome Hartmann braking. Rather than try to untangle the effects of the additional terms in the PSM model from small differences in solutions that are dominated by forcing and dissipation, we shall just discard the linear drag and forcing terms from (1.6), the terms that coincide with those obtained previously by Sommeria & Moreau (1982), and investigate the effect of the extra terms in the PSM model on freely decaying turbulence. Moreover, the anticipated vorticity method and its variations that we wish to compare with the PSM model have no linear drag terms.

2. The PSM model

The model due to PSM describes magnetohydrodynamic flow in a thin layer of liquid metal permeated by a vertical magnetic field. The underlying three-dimensional equations are the Navier–Stokes equation with the Lorentz force,

$$\partial_t \boldsymbol{u}_3 + \boldsymbol{u}_3 \cdot \nabla_3 \boldsymbol{u}_3 + \nabla_3 p = \nu_* \nabla_3^2 \boldsymbol{u}_3 + \boldsymbol{J} \times \boldsymbol{B}, \tag{2.1}$$

combined with Ohm's law

$$\eta_* \boldsymbol{J} = -\nabla_3 \phi + \boldsymbol{u}_3 \times \boldsymbol{B}, \tag{2.2}$$

to determine the current $\boldsymbol{J} = \nabla \times \boldsymbol{B}$. We use $\boldsymbol{u}_3$ for the three-dimensional velocity field, in contrast to the $\boldsymbol{u}$ used elsewhere for the horizontal velocity only, and ∇_3 to denote the three-dimensional gradient operator. In liquid-metal magnetohydrodynamics, the magnetic Reynolds number $Rm = UL/\eta_*$ is usually small enough to neglect variations in the magnetic field $\boldsymbol{B} = \boldsymbol{B}_0 + O(Rm)$ from its applied value $\boldsymbol{B}_0 = B_0 \hat{\boldsymbol{z}}$, which we take to be spatially uniform. The Lorentz force $\boldsymbol{J} \times \boldsymbol{B}$ therefore linearizes to $B_0 \boldsymbol{J} \times \hat{\boldsymbol{z}}$, and Ohm's law linearizes to $\eta_* \boldsymbol{J} = -\nabla_3 \phi + B_0 \boldsymbol{u}_3 \times \hat{\boldsymbol{z}}$, from which we deduce (Roberts 1967, p. 137)

$$\partial_t \boldsymbol{u}_3 + \boldsymbol{u}_3 \cdot \nabla_3 \boldsymbol{u}_3 + \nabla_3 p = \nu_* \nabla_3^2 \boldsymbol{u}_3 - \frac{B_0^2}{\rho \eta_*} \nabla_3^{-2} \frac{\partial^2 \boldsymbol{u}_3}{\partial z^2}. \tag{2.3}$$

The inverse three-dimensional Laplace operator ∇_3^{-2} in (2.3) acquires its boundary conditions from the normal current $\boldsymbol{J} \cdot \boldsymbol{n}$ on the boundary. The last term in (2.3) has the effect of 'diffusing' away spatial variations in the z-direction (Davidson 1995). For parameters typical of liquid metals at laboratory scales these variations diffuse very quickly by comparison with an eddy turnover time, thus establishing a quasi-two-dimensional flow away from no-slip boundaries (Sommeria & Moreau 1982).

Alternatively, the Fourier transform of (2.3) may be analysed in terms of wave vectors (Alemany *et al.* 1979; Sommeria & Moreau 1982; Moreau 1998). Unlike the usual case of isotropic hydrodynamic turbulence, the magnetic field imposes a preferred direction so it is necessary to consider wave vectors rather than just scalar wavenumbers. The Fourier interpretation of the last term in (2.3) is that resistivity only dissipates wavenumbers inclined to the imposed magnetic field, and thus causes three-dimensional modes to decay more rapidly than purely two-dimensional modes. Moreover, the electrical boundary conditions on the upper and lower boundaries have the effect of quantizing the permissible wave vectors. In the case of insulating boundaries, the vertical wavenumber must be $k_z = n\pi/a$ for some integer n (Sommeria & Moreau 1982; Moreau 1998), so there are no 'almost two-dimensional' wave vectors. The resistive damping of three-dimensional modes is offset by the usual transfer of energy between modes by the nonlinear $\boldsymbol{u}_3 \cdot \nabla_3 \boldsymbol{u}_3$ inertial term. This sets constraints on the permissible strength of inertia, as measured by the interaction parameter N, such that quasi-two-dimensional magnetohydrodynamics is valid for horizontal wavenumbers k with $ka \ll N^{-1/3}$ (Sommeria 1988).

In suitable dimensionless variables, the layer average of the horizontal components of equation (2.1) may be rewritten as (PSM)

$$\partial_t \overline{\boldsymbol{u}} + \overline{\boldsymbol{u}} \cdot \nabla \overline{\boldsymbol{u}} + \overline{\boldsymbol{u}' \cdot \nabla \boldsymbol{u}'} + \nabla \overline{p} = \frac{N\delta}{Ha^2} \nabla^2 \overline{\boldsymbol{u}} + \frac{N}{Ha^2 \delta} \boldsymbol{\tau}_{\mathrm{w}} + \frac{N}{Ha\,\delta} \boldsymbol{u}_0, \tag{2.4}$$

where $\boldsymbol{u}_3 = (\boldsymbol{u}, w)$ and $\boldsymbol{J} = (\boldsymbol{j}, j_z)$ have been decomposed into horizontal and vertical components. An overbar denotes a layer average, and $\boldsymbol{u}' = \boldsymbol{u} - \overline{\boldsymbol{u}}$ denotes the deviation in velocity away from this average. The parameters appearing in (2.4) are the Hartmann number Ha, as defined above, the interaction parameter $N = B_0^2 a/(\rho \eta_* U)$,

and the aspect ratio δ. The vertically averaged Lorentz force $\overline{\boldsymbol{j}} \times \hat{\boldsymbol{z}}$ may be written as a two-dimensional velocity field $Ha^{-1}\boldsymbol{u}_0$, one that is determined by current injection at the boundaries (Sommeria 1986). The remaining quantities necessary to close the equation are the Reynolds stress $\overline{\boldsymbol{u}' \cdot \nabla \boldsymbol{u}'}$ due to vertical variations in the velocity, and the wall stress $\boldsymbol{\tau}_{\mathrm{w}}$.

These quantities are determined predominantly by the Hartmann layers at the walls. In contrast to the core flow, the Hartmann layers are dominated by a balance between viscosity and the Lorentz force. The horizontal velocity inside the Hartmann layer is approximately

$$\boldsymbol{u}_3(\boldsymbol{x}, \xi) = \boldsymbol{u}_{\mathrm{c}}(1 - \mathrm{e}^{-\xi}) + \frac{\delta}{N}\left[\left(\tfrac{1}{3}\mathrm{e}^{-2\xi} - \tfrac{1}{3}\mathrm{e}^{-\xi} + \xi \mathrm{e}^{-\xi}\right)\boldsymbol{u}_{\mathrm{c}} \cdot \nabla \boldsymbol{u}_{\mathrm{c}} + \tfrac{1}{2}\xi \mathrm{e}^{-\xi}\partial_t \boldsymbol{u}_{\mathrm{c}}\right], \quad (2.5)$$

where $\xi = zHa$ is a rescaled vertical coordinate inside the Hartmann layer, and $\boldsymbol{u}_{\mathrm{c}}$ denotes the velocity in the core, so that $\boldsymbol{u}_3(\boldsymbol{x}, \xi) \to \boldsymbol{u}_{\mathrm{c}}(\boldsymbol{x})$ as $\xi \to \infty$. The first and largest term in equation (2.5) is the usual linear Hartmann layer velocity profile, as sketched in figure 1. The other terms are inertial corrections to the dominant balance of Lorentz, viscous, and pressure forces in the Hartmann layer.

The average velocity $\overline{\boldsymbol{u}}$ is thus related to the core velocity $\boldsymbol{u}_{\mathrm{c}}$ appearing in equation (2.5) by

$$\boldsymbol{u}_{\mathrm{c}} = \left(1 + \frac{n}{Ha}\right)\overline{\boldsymbol{u}} - \frac{n\,\delta}{Ha\,N}\left(\tfrac{5}{6}\overline{\boldsymbol{u}} \cdot \nabla \overline{\boldsymbol{u}} + \tfrac{1}{2}\partial_t \overline{\boldsymbol{u}}\right) + O(Ha^{-2}N^{-2}). \quad (2.6)$$

The extra factor of nHa^{-1} appears because deviations from the core velocity are confined to n Hartmann layers of width Ha^{-1}. Equation (2.6) may be used to eliminate $\boldsymbol{u}_{\mathrm{c}}$ from (2.5), and subsequently to calculate the wall stress $\boldsymbol{\tau}_{\mathrm{w}}$ and the vertically averaged Reynolds stress $\overline{\boldsymbol{u}' \cdot \nabla \boldsymbol{u}'}$. After rescaling $\overline{\boldsymbol{u}}$ and t to absorb constants, PSM finally obtained a closed equation for the rescaled vertically averaged velocity $\overline{\boldsymbol{u}}$,

$$\partial_t \overline{\boldsymbol{u}} + \overline{\boldsymbol{u}} \cdot \nabla \overline{\boldsymbol{u}} + \nabla p = \frac{N\,\delta}{Ha^2}\nabla^2 \overline{\boldsymbol{u}} + \frac{N}{Ha\,\delta}(\overline{\boldsymbol{u}}_0 - n\alpha\overline{\boldsymbol{u}}) + \frac{n\,\delta}{Ha\,N}\left(\tfrac{7}{36}\mathscr{D}_{\overline{\boldsymbol{u}}} + \tfrac{1}{8}\partial_t\right)\overline{\boldsymbol{u}} \cdot \nabla \overline{\boldsymbol{u}}, \quad (2.7)$$

subject to $\nabla \cdot \overline{\boldsymbol{u}} = 0$, which coincides with (1.6) above after identifying the dimensionless groups in (1.7), and absorbing $n\alpha$ into the drag coefficient and $\overline{\boldsymbol{u}}_0$. The linear operator $\mathscr{D}_{\overline{\boldsymbol{u}}}$ is defined by $\mathscr{D}_{\overline{\boldsymbol{u}}}\boldsymbol{F} = \overline{\boldsymbol{u}} \cdot \nabla \boldsymbol{F} + \boldsymbol{F} \cdot \nabla \overline{\boldsymbol{u}}$ as in (1.5) above.

The additional nonlinear terms on the right-hand side of (2.7) describe the effects of inertial corrections to flow in the Hartmann layers. The easiest case to interpret physically is an axisymmetric recirculating flow or vortex, which requires an inward radial pressure gradient to balance the centrifugal force. This pressure gradient is pressed into the Hartmann boundary layers, since the usual small-aspect-ratio scaling implies that the pressure must be uniform across a boundary layer, and drives a small radial inflow inside the Hartmann layers. By mass conservation, the inflow must be balanced by a radial outflow in the core, giving rise to the usual recirculating flow in a vertical plane called Ekman pumping. Since there is no net inward or outward mass flux the Ekman pumping makes no contribution to the vertically averaged velocity $\overline{\boldsymbol{u}}$. However, the horizontal leading-order flow is weaker in the boundary layers than in the core, as sketched in figure 1, due to the no-slip boundary conditions. The outward transport of the leading-order flow by the secondary flow in the core is thus larger than the inward transport in the boundary layers, leading to a net outward transport of the vertically averaged velocity $\overline{\boldsymbol{u}}$, despite there being no net outward component of the velocity. This physical mechanism is well understood for axisymmetric flows, and is responsible for the increased spreading of steady, strong vortices driven by current

injection (Sommeria 1988; PSM). Its extension to unsteady, non-axisymmetric flows, as captured in a layer-averaged model by the PSM equation, will be investigated in this paper.

For axisymmetric flows that decay at infinity, the PSM equation may be rewritten as

$$\Gamma_t = \nu \left(\Gamma_{rr} - \frac{1}{r}\Gamma_r \right) + \kappa(\Gamma_0 - \Gamma) - \frac{7\beta}{144\pi^2} \frac{1}{r^3}\Gamma^2\Gamma_r, \tag{2.8}$$

in terms of the circulation Γ given by

$$\Gamma(r,t) = 2\pi r u_\theta = 2\pi \int_0^r r'\omega(r',t)\,\mathrm{d}r', \tag{2.9}$$

and where Γ_0 is the corresponding function calculated from the forcing vorticity ω_0 as determined by the injected currents. Equation (2.8) thus follows from the streamfunction–vorticity form (1.8) of the PSM equation by multiplying by r and integrating. The Jacobian $[\psi,\omega]=0$ for axisymmetric flows, so the anisotropic diffusion term $[\psi,[\psi,\omega]]$ and the implicit term $\partial_t[\psi,\omega]$ in the PSM equation both vanish. Similar equations for steady axisymmetric flows were obtained by PSM, and used to calculate the response to forcing from a point current source, as in the experiments of Sommeria (1988).

A further change of spatial coordinate from r to s, where

$$s = \left(\frac{108\pi^2}{7\beta} \right) r^4, \tag{2.10}$$

transforms (2.8) into

$$\Gamma_t + (\Gamma^3)_s = \kappa(\Gamma_0 - \Gamma) + \nu \frac{96\sqrt{3}\pi}{\sqrt{7\beta}} \left(s^{3/2}\Gamma_{ss} + \tfrac{1}{2}s^{1/2}\Gamma_s \right). \tag{2.11}$$

The $(\Gamma^3)_s$ term on the left-hand side arises from the outward transport of vorticity by the Ekman pumping mechanism described above. In these axisymmetric incompressible flows the radial velocity is zero everywhere (assuming no mass source at the origin) but there is nevertheless a radial transport of the azimuthal velocity or circulation. In the absence of forcing, drag, and viscosity ($\kappa=0$ and $\nu=0$) equation (2.11) has self-similar solutions corresponding to expanding patches of uniform vorticity in a quiescent fluid. These solutions, and their modifications by forcing and viscosity, will be explored in a future paper.

2.1. *An explicit version of the PSM equation*

Since PSM have already substituted $\bar{\boldsymbol{u}}$ for $\boldsymbol{u}_c$ at leading order in equation (2.6) to calculate the first-order inertial corrections, to the same order of accuracy we may approximate $\partial_t\boldsymbol{u}$ using the Euler equation with forcing and drag, $\partial_t\boldsymbol{u} = -(\boldsymbol{u}\cdot\nabla\boldsymbol{u} + \nabla p') + \kappa(\boldsymbol{u}_0 - \boldsymbol{u}) + O(\nu) + O(\beta)$, to obtain

$$\partial_t\boldsymbol{u} + \left(1 + \tfrac{1}{8}\beta\kappa\right)\boldsymbol{u}\cdot\nabla\boldsymbol{u} + \nabla p = \nu\nabla^2\boldsymbol{u} + \kappa(\boldsymbol{u}_0 - \boldsymbol{u})$$
$$+ \tfrac{5}{72}\beta\mathscr{D}_{\boldsymbol{u}}(\boldsymbol{u}\cdot\nabla\boldsymbol{u}) - \tfrac{1}{8}\beta\mathscr{D}_{\boldsymbol{u}}\nabla p' + \tfrac{1}{8}\beta\kappa\mathscr{D}_{\boldsymbol{u}}\boldsymbol{u}_0. \quad (2.12)$$

The auxiliary pressure p' is determined by $\nabla\cdot(\boldsymbol{u}\cdot\nabla\boldsymbol{u} + \nabla p')=0$ to ensure that the approximation for $\partial_t\boldsymbol{u}$ is incompressible, and will differ from the true pressure p by corrections of $O(\nu)$ and $O(\beta)$. We may obtain a simpler closed-form equation using the alternative streamfunction–vorticity formulation from the introduction. Substituting

the leading-order vorticity equation $\omega_t = -[\psi, \omega] + \kappa(\omega_0 - \omega) + O(\nu) + O(\beta)$ to eliminate the implicit $\partial_t[\psi, \omega]$ term transforms (1.8) into

$$\partial_t \omega + \left(1 + \tfrac{1}{8}\beta\kappa\right)[\psi, \omega] = \nu\nabla^2\omega + \kappa(\omega_0 - \omega) - \tfrac{1}{8}\beta[\nabla^{-2}[\psi, \omega], \omega]$$
$$+ \tfrac{5}{72}\beta[\psi, [\psi, \omega]] + \tfrac{7}{36}\beta\{[\psi_y, \omega\psi_x] + [\omega\psi_y, \psi_x]\} + \tfrac{1}{8}\beta\kappa\{[\psi, \omega_0] + [\psi_0, \omega]\}, \quad (2.13)$$

where $\psi_0 = \nabla^{-2}\omega_0$. These two different forms will be useful for estimating the evolution of the energy in §5.

The implicit nature of the original PSM model is interesting, and theoretically beneficial. As with any shallow-layer approximation, PSM's equation cannot be expected to remain valid for arbitrarily small horizontal lengthscales, because the small aspect ratio assumption breaks down when $k\delta = O(1)$, k being a typical dimensionless horizontal wavenumber. For this reason Benjamin, Bona & Mahony (1972) argued that it is desirable for the approximate long-wave equation to have some "innocuous" behaviour in the short-wave limit, and in particular that the decay rates and phase speeds for linear waves should not diverge like k^2 or higher powers of k as $k \to \infty$. The decay rate for linear waves is found in §6 to be bounded as $k \to \infty$ for PSM's equation (1.8), but to diverge as k^2 for the explicit version given in equation (2.13). However, this difference only becomes apparent for large wavenumbers with $k \sim \beta^{-1}$, as shown in §6. These wavenumbers are not resolved by the numerical experiments reported below, so the computed solutions of the explicit and implicit versions of the PSM equation are almost identical.

The existence of rapidly decaying fluctuations may impose a severe timestep constraint on numerical methods. When simulating the plain Navier–Stokes equations it is common to use some unconditionally stable numerical scheme to integrate the viscous terms, such as Crank–Nicolson, or the "backward time stepping" used by Verron & Sommeria (1987). Although they remain stable, these numerical schemes usually become inaccurate for rapidly decaying modes. In particular Crank–Nicolson causes modes that should decay very rapidly over a timestep in the original PDE to decay hardly at all in the numerical solution, but instead to oscillate with almost constant amplitude. Thus many numerical implementations have the effect of reducing the decay rate of high-wavenumber modes, which is similar to the way the original PSM equation modifies the decay rate of high-wavenumber modes compared with the explicit version (2.13), but is hidden in the numerical implementation instead of made apparent by changing the equations. The implementation of an unconditionally stable numerical scheme like Crank–Nicolson also becomes much more complicated for the nonlinear diffusion terms present in all three modified equations, since the algebraic equations determining the dependent variables at the end of the timestep become nonlinear, and typically have to be solved by Newton's method. Numerical solutions of the implicit and explicit versions of the PSM equation thus require algorithms of similar complexity, as explained in §7 below. It turns out that for realistic laboratory parameters the primary constraint on the timestep is the accuracy of the advection rather than any stability constraint for diffusion.

2.2. *Comparison with other shallow-layer magnetohydrodynamic equations*

It is perhaps worth contrasting equation (2.7) with the dispersive shallow-water magnetohydrodynamic (SWMHD) equations recently obtained by Dellar (2003) to model a thin layer of electrically conducting fluid permeated by a predominantly horizontal magnetic field at high magnetic Reynolds number. Dispersive SWMHD extends Gilman's (2000) earlier SWMHD equations by retaining higher-order terms

in a small aspect ratio approximation, and coincides with Green & Naghdi's (1976) higher-order shallow-water equations in the absence of a magnetic field. All these equations may be derived by layer-averaging. The chief difference between these models and the PSM equation arises because SWMHD neglects viscous and resistive effects. SWMHD therefore lacks the Hartmann boundary layers that define a (small) vertical lengthscale other than the layer depth. In particular, the leading-order horizontal velocity in Green–Naghdi or dispersive SWMHD is independent of z throughout the domain, so the vertically averaged Reynolds stress is simply $\overline{uu} = \overline{u}\,\overline{u}$ to sufficient accuracy. Corrections similar to the last term in equation (2.7) only arise via non-hydrostatic contributions to the pressure. These corrections are dispersive rather than dissipative, involving odd rather than even numbers of derivatives, but still lead to an implicit system containing mixed spatio-temporal derivatives.

3. The anticipated vorticity method

The qualitative behaviour of the two-dimensional Navier–Stokes equations is strongly constrained by the behaviour of the kinetic energy $\mathscr{E}$, and enstrophy (mean squared vorticity) $\mathscr{Z}$, as given by

$$\mathscr{E} = \frac{1}{2} \int |\boldsymbol{u}|^2 \, \mathrm{d}x \, \mathrm{d}y = -\frac{1}{2} \int \omega \psi \, \mathrm{d}x \, \mathrm{d}y, \quad \mathscr{Z} = \frac{1}{2} \int \omega^2 \, \mathrm{d}x \, \mathrm{d}y. \qquad (3.1)$$

We have assumed suitable boundary conditions, such as periodic or no flux ($\psi = 0$ on the boundary), to integrate by parts on the energy integral. Both quantities are exactly conserved by the two-dimensional Euler equations ($\nu = 0$).

The selective decay property of two-dimensional turbulence is based on the observation that for the Navier–Stokes equations ($\nu > 0$),

$$\frac{\mathrm{d}\mathscr{E}}{\mathrm{d}t} = -\nu \int |\omega|^2 \, \mathrm{d}x \, \mathrm{d}y = -2\nu \mathscr{Z} = O(\nu) \text{ as } \nu \to 0, \qquad (3.2a)$$

$$\frac{\mathrm{d}\mathscr{Z}}{\mathrm{d}t} = -\nu \int |\nabla \omega|^2 \, \mathrm{d}x \, \mathrm{d}y = O(\nu^\gamma) \text{ with } \gamma < 1, \qquad (3.2b)$$

because $|\omega|$ and $\mathscr{Z}$ are bounded independently of ν by the initial conditions (Batchelor 1969; Bretherton & Haidvogel 1976; Matthaeus & Montgomery 1980). By contrast, vortex stretching in three dimensions typically causes enstrophy to grow initially rather than decay. Numerical simulations by Kida, Yamada & Ohkitani (1988) suggest that $\gamma \approx 0$ in fully developed two-dimensional turbulence, whereas $\gamma \approx 1/2$ when regions of strong vorticity gradients are confined to a few one-dimensional structures, or sheets. In either case, the enstrophy $\mathscr{Z}$ decays at an asymptotically faster rate than the energy $\mathscr{E}$ as $\nu \to 0$. Ting, Matthaeus & Montgomery (1986) gave a concrete proof that $\partial_t(\mathscr{Z}/\mathscr{E}) \leqslant 0$ in a periodic domain, with equality only for flows comprising a single Fourier mode.

The anticipated vorticity method proposed by Sadourny & Basdevant (1981, 1985, see also Basdevant & Sadourny 1983) is a model for two-dimensional turbulence motivated by the asymptotically rapid decay of enstrophy with respect to energy at high Reynolds numbers, or small ν. As in many turbulence models, they decomposed the velocity and vorticity into mean and fluctuating parts,

$$\boldsymbol{u} = \overline{\boldsymbol{u}} + \boldsymbol{u}', \quad \omega = \overline{\omega} + \omega', \qquad (3.3)$$

where $\overline{\boldsymbol{u}}$ and $\overline{\omega}$ are supposed to arise from applying some local averaging procedure to the true fields $\boldsymbol{u}$ and ω. In this section an overbar means a small-scale average, not

a layer average. These averages are supposed to be resolved by numerical simulations, while the remaining fluctuations $\boldsymbol{u}' = \boldsymbol{u} - \overline{\boldsymbol{u}}$ and $\omega' = \omega - \overline{\omega}$ are supposed to contain unresolved small lengthscales. Thus the vorticity equation becomes

$$\partial_t(\overline{\omega} + \omega') + \overline{\boldsymbol{u}} \cdot \nabla \overline{\omega} + \overline{\boldsymbol{u}} \cdot \nabla \omega' + \boldsymbol{u}' \cdot \nabla \overline{\omega} + \boldsymbol{u}' \cdot \nabla \omega' = \nu \nabla^2 (\overline{\omega} + \omega'). \tag{3.4}$$

Assuming a forward enstrophy cascade at small scales, and a corresponding k^{-3} spectrum (Kraichnan 1967) for the energy at wavenumber k, implies the inequalities $\boldsymbol{u}' \cdot \nabla \omega' \ll \overline{\boldsymbol{u}} \cdot \nabla \omega'$ and $\boldsymbol{u}' \cdot \nabla \overline{\omega} \ll \overline{\boldsymbol{u}} \cdot \nabla \omega'$. Ignoring viscosity, the leading-order mean vorticity equation is thus

$$\partial_t \overline{\omega} + \overline{\boldsymbol{u}} \cdot \nabla(\overline{\omega} + \omega') = 0. \tag{3.5}$$

Sadourny & Basdevant (1981, 1985) postulated an equation for the vorticity fluctuations of the form

$$\partial_t \omega' + \frac{\lambda}{\tau}(\overline{\boldsymbol{u}} \cdot \nabla \overline{\omega}) = -\frac{\omega'}{\tau}, \tag{3.6}$$

where ω' is forced by the mean vorticity gradient, but relaxes back towards zero with some timescale τ. Equation (3.6) formally simplifies to $\omega' = -\lambda \overline{\boldsymbol{u}} \cdot \nabla \overline{\omega}$ in the small-relaxation-time limit $\tau \to 0$, after which equation (3.5) becomes the inviscid anticipated vorticity equation

$$\partial_t \overline{\omega} + \overline{\boldsymbol{u}} \cdot \nabla(\overline{\omega} - \lambda \overline{\boldsymbol{u}} \cdot \nabla \overline{\omega}) = 0. \tag{3.7}$$

The energy equation (3.2*a*) is unchanged by the extra term, while the enstrophy equation becomes

$$\frac{\mathrm{d}\mathscr{L}}{\mathrm{d}t} = -\int \mathrm{d}x \, \mathrm{d}y \, \nu \, |\nabla \overline{\omega}|^2 + \lambda \, |\overline{\boldsymbol{u}} \cdot \nabla \overline{\omega}|^2. \tag{3.8}$$

4. The anticipated velocity method

As noted in the Introduction, the evolution equation for $\boldsymbol{u}$ implied by the anticipated vorticity equation (3.7) for ω cannot be written as the divergence of a symmetric stress tensor. For this reason, Benzi *et al.* (1990, 1992) proposed the alternative

$$\partial_t \boldsymbol{u} + \boldsymbol{u} \cdot \nabla \boldsymbol{u} + \nabla p = \lambda \nabla \cdot \{\boldsymbol{u}(\boldsymbol{u} \cdot \nabla \boldsymbol{u}) + (\boldsymbol{u} \cdot \nabla \boldsymbol{u})\boldsymbol{u}\} \tag{4.1}$$

as being more suitable for implementation in a lattice Boltzmann method (Benzi *et al.* 1992; Chen & Doolen 1998; Succi 2001). In these simplified versions of the kinetic theory of gases, macroscopic quantities like fluid density and velocity are derived from a set of distribution functions f_i that are postulated to evolve according to a lattice Boltzmann equation of the form

$$\partial_t f_i + \boldsymbol{\xi}_i \cdot \nabla f_i = \mathscr{C}_i(f_0, \dots, f_N). \tag{4.2}$$

The constant lattice vectors $\boldsymbol{\xi}_i$ and collision operator $\mathscr{C}$ must be chosen so that the first few moments of equation (4.2) give the required macroscopic equations in the form

$$\partial_t \rho + \nabla \cdot (\rho \boldsymbol{u}) = 0, \quad \partial_t(\rho \boldsymbol{u}) + \nabla \cdot \boldsymbol{\Pi} = 0. \tag{4.3}$$

In particular, since the momentum equation is derived by multiplying equation (4.2) by $\boldsymbol{\xi}_i$ and summing, the momentum flux tensor $\boldsymbol{\Pi} = \sum_i \boldsymbol{\xi}_i \boldsymbol{\xi}_i f_i$ is symmetric by construction.

Dellar (2004) devised a lattice Boltzmann equation that solved the compressible analogue of the anticipated velocity method in the form

$$\partial_t \rho + \nabla \cdot (\rho \boldsymbol{u}) = 0, \tag{4.4a}$$

$$\partial_t(\rho \boldsymbol{u}) + \nabla \cdot \left(c_s^2 \rho \boldsymbol{I} + \rho \boldsymbol{u}\boldsymbol{u} - \lambda \rho [(\boldsymbol{u} \cdot \nabla \boldsymbol{u})\boldsymbol{u} + \boldsymbol{u}(\boldsymbol{u} \cdot \nabla \boldsymbol{u})] \right) = \nabla \cdot [\rho \nu ((\nabla \boldsymbol{u}) + (\nabla \boldsymbol{u})^{\mathrm{T}})], \tag{4.4b}$$

where $c_s^2 \rho \boldsymbol{I}$ is the isotropic pressure tensor for an isothermal equation of state with sound speed c_s. This equation of state arises in the simplest and most commonly used lattice Boltzmann equations (Chen & Doolen 1998). Solutions of this system are expected to converge towards solutions of the incompressible equation (4.1) in the limit of small Mach number, $Ma = |\boldsymbol{u}|/c_s \rightarrow 0$. Dellar (2004) also showed that the continuum equations solved by most common lattice Boltzmann equations, using nine particle velocities $\boldsymbol{\xi}_i$ arranged on a square lattice, coincide with the anticipated velocity method with a small negative (antidiffusive) value of λ. The compressible solutions reported in Dellar (2004) converge with the expected $O(Ma^2)$ compressibility error, and second-order spatial truncation error, towards the incompressible solutions obtained using the numerical method described in §7 below. These solutions provide an independent verification of the numerical method and solutions presented in this paper.

5. Evolution of energy and enstrophy under the PSM model

In this section we consider the evolution of the energy and enstrophy under the PSM equation without forcing or drag. These terms proportional to κ that we neglect would add extra algebraic terms to the energy and enstrophy dissipation rates. Taking the inner product of the dimensionless PSM equation (1.6) with $\boldsymbol{u}$ and integrating by parts leads to an energy equation in the form

$$\frac{\mathrm{d}\mathscr{E}}{\mathrm{d}t} = -\int \mathrm{d}x\,\mathrm{d}y \; \nu\,\omega^2 + \tfrac{7}{36}\beta|\boldsymbol{u} \cdot \nabla \boldsymbol{u}|^2 + \tfrac{1}{8}\beta(\boldsymbol{u} \cdot \nabla \boldsymbol{u}) \cdot \frac{\partial \boldsymbol{u}}{\partial t}. \tag{5.1}$$

The time derivative has been moved from $\boldsymbol{u} \cdot \nabla \boldsymbol{u}$ onto $\boldsymbol{u}$ in the last term using the formula $\boldsymbol{u} \cdot \partial_t(\boldsymbol{u} \cdot \nabla \boldsymbol{u}) = \partial_t(\nabla \cdot (\tfrac{1}{2}|\boldsymbol{u}|^2 \boldsymbol{u})) - (\boldsymbol{u} \cdot \nabla \boldsymbol{u}) \cdot \partial_t \boldsymbol{u}$. The exact time derivative $\partial_t()$ vanishes because it is the time derivative of an exact spatial divergence. Equation (5.1) may be rewritten as

$$\frac{\mathrm{d}\mathscr{E}}{\mathrm{d}t} = -\int \mathrm{d}x\,\mathrm{d}y \; \left(\nu\,\omega^2 + \tfrac{5}{72}\beta|\boldsymbol{u} \cdot \nabla \boldsymbol{u}|^2 \right) + \tfrac{1}{8}\beta \int \mathrm{d}x\,\mathrm{d}y \; ((\boldsymbol{u} \cdot \nabla \boldsymbol{u}) \cdot \nabla p') + O(\beta^2, \beta\nu, \nu^2), \tag{5.2}$$

after substituting the leading-order approximation $\partial_t \boldsymbol{u} = -\boldsymbol{u} \cdot \nabla \boldsymbol{u} - \nabla p' + O(\beta, \nu)$ consistent with the neglect of forcing and drag. The pressure p' ensures that the approximate $\partial_t \boldsymbol{u}$ is incompressible, and differs by $O(\beta, \nu)$ from the true pressure p in (1.6). The Poisson equation $\nabla^2 p' = -\nabla \cdot (\boldsymbol{u} \cdot \nabla \boldsymbol{u})$ that defines p' allows the second integral in (5.2) to be manipulated into

$$\int \mathrm{d}x\,\mathrm{d}y \; (\boldsymbol{u} \cdot \nabla \boldsymbol{u}) \cdot \nabla p' = -\int \mathrm{d}x\,\mathrm{d}y \; p' \nabla \cdot (\boldsymbol{u} \cdot \nabla \boldsymbol{u})$$

$$= \int \mathrm{d}x\,\mathrm{d}y \; p' \nabla^2 p' = -\int \mathrm{d}x\,\mathrm{d}y \; |\nabla p'|^2 \leqslant 0. \tag{5.3}$$

Equation (5.2) then implies the energy inequality

$$\frac{\mathrm{d}\mathscr{E}}{\mathrm{d}t} \leqslant -\int \mathrm{d}x\,\mathrm{d}y\ \left(\nu\,\omega^2 + \tfrac{5}{72}\beta|\boldsymbol{u}\cdot\nabla\boldsymbol{u}|^2\right) \leqslant 0, \tag{5.4}$$

ignoring errors of quadratic order in β and ν. In other words, the extra nonlinear terms in the PSM equation due to Ekman pumping cause energy to decrease as expected, at least when the deviations from the two-dimensional Euler equations are small enough to justify simplifying the $\partial_t(\boldsymbol{u}\cdot\nabla\boldsymbol{u})$ term using a leading-order approximation for $\partial_t\boldsymbol{u}$.

The energy equation (5.2) based on the leading-order approximation for $\partial_t\boldsymbol{u}$ may also be rewritten in streamfunction–vorticity form as

$$\frac{\mathrm{d}\mathscr{E}}{\mathrm{d}t} = -\int \mathrm{d}x\,\mathrm{d}y\ \nu\,\omega^2 + \tfrac{7}{36}\beta\left([\psi,\psi_x]^2 + [\psi,\psi_y]^2\right) + \tfrac{1}{8}\beta[\psi,\omega]\nabla^{-2}\left([\psi,\omega]\right). \tag{5.5}$$

While the final term has the opposite sign to the first two, because ∇^{-2} is a negative definite operator, the previous argument about the pressure ensures that it is always dominated by the second term. The energy decay rate thus satisfies the inequalities

$$\int \mathrm{d}x\,\mathrm{d}y\ \left(\nu\,\omega^2 + \tfrac{5}{72}\beta|\boldsymbol{u}\cdot\nabla\boldsymbol{u}|^2\right) \leqslant -\frac{\mathrm{d}\mathscr{E}}{\mathrm{d}t} \leqslant \int \mathrm{d}x\,\mathrm{d}y\ \left(\nu\,\omega^2 + \tfrac{7}{36}\beta|\boldsymbol{u}\cdot\nabla\boldsymbol{u}|^2\right). \tag{5.6}$$

We return to these inequalities in the light of some numerical experiments in §9 below.

The corresponding enstrophy equation for the explicit form of the PSM equation is

$$\frac{\mathrm{d}\mathscr{Z}}{\mathrm{d}t} = -\int \mathrm{d}x\,\mathrm{d}y\ \nu\,|\nabla\omega|^2 + \tfrac{5}{72}\beta[\psi,\omega]^2 + \tfrac{7}{36}\beta\omega^2[\psi_x,\psi_y], \tag{5.7}$$

in streamfunction–vorticity notation. The enstrophy need not decay monotonically, and may in fact increase. An explicit example is $\psi = r^2/(1+r^2)^2$ in polar coordinates. Since ψ and ω are both functions of the polar radius r only, the Jacobian term $[\psi,\omega]^2$ in (5.7) vanishes. The final term dominates the integral when ν/β is sufficiently small, making $\partial_t\mathscr{Z}$ positive. In general, streamfunctions of this form that correspond to a reversal in the sign of the circulation (as in §2) lead to shock formation in the inviscid, drag-free form of the axisymmetric PSM equation.

For comparison, the energy and enstrophy equations for the anticipated velocity method are

$$\frac{\mathrm{d}\mathscr{E}}{\mathrm{d}t} = -\int \mathrm{d}x\,\mathrm{d}y\ (\nu\,\omega^2 + \lambda|\boldsymbol{u}\cdot\nabla\boldsymbol{u}|^2) \leqslant 0, \tag{5.8}$$

which lacks the time-derivative term in (5.1), and

$$\frac{\mathrm{d}\mathscr{Z}}{\mathrm{d}t} = -\int \mathrm{d}x\,\mathrm{d}y\ \nu|\nabla\omega|^2 + \lambda([\psi,\omega]^2 + \omega^2[\psi_x,\psi_y] + 2\omega\nabla\cdot([\psi_x,\psi_y]\nabla\psi)). \tag{5.9}$$

Thus the anticipated velocity method dissipates energy, like the PSM equation, but may cause enstrophy to increase, again like the PSM equation. By contrast, the anticipated vorticity method leaves the energy invariant, and dissipates enstrophy.

6. Linear waves

To analyse further the properties of the PSM equation (1.6), again without forcing or drag, we consider the behaviour of small-amplitude waves on a uniform background flow. Taking the uniform flow to be in the positive x-direction, so that
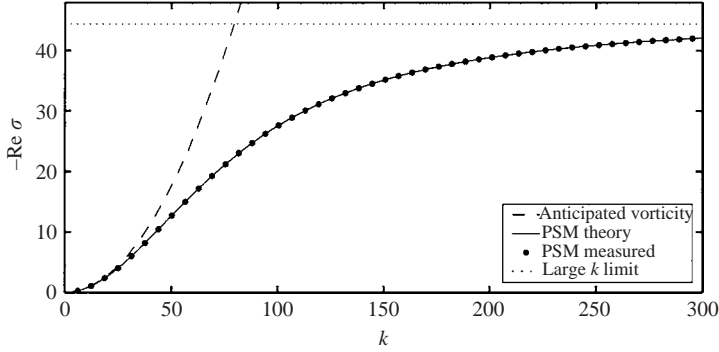
FIGURE 2. Decay rate $-\mathrm{Re}\,\sigma$ versus wavenumber k for the PSM model with $U = 1$, $\beta = 0.1$, and $\nu = 10^{-4}$. The solid line is the theoretical prediction from equation (6.1), and the dots are numerical measurements from simulations (see §8.1). The upper dotted line is the large-wavenumber limit, $-\mathrm{Re}\,\sigma \to 40/(9\beta) + 64\nu/(\beta U)^2$ as $k \to \infty$. The dashed parabola shows the theoretical prediction for all of the explicit methods: anticipated vorticity, anticipated velocity, and the explicit PSM equation (2.13).

$\psi = -Uy + \psi'(x, y, t)$, linear plane wave solutions with ψ' proportional to $\exp[\sigma t + \mathrm{i}(kx + ly)]$ exist with growth rate

$$\sigma = -\mathrm{i}kU \frac{1 + \frac{1}{8}\beta\nu(k^2 + l^2) + \frac{7}{288}\beta^2 k^2 U^2}{1 + \frac{1}{64}\beta^2 k^2 U^2} - \frac{\nu(k^2 + l^2) + \frac{5}{72}\beta k^2 U^2}{1 + \frac{1}{64}\beta^2 k^2 U^2}. \tag{6.1}$$

The real part of σ, which is negative, determines the decay rate, while the imaginary part determines the propagation speed. The decay rate initially increases proportionally to k^2, but eventually saturates at the finite value $40/(9\beta) + 64\nu/(\beta U)^2$ as $k \to \infty$, as shown in figure 2. Ignoring viscosity, the group velocity $\mathrm{d}(\mathrm{Im}\,\sigma)/\mathrm{d}k$ reaches a maximum of $13U/8$ at $k = 8\sqrt{3}/(\beta U)$, and then asymptotes to the lower value of $14U/9$ as $k \to \infty$. The phase velocity $k^{-1}\mathrm{Im}\,\sigma$ increases monotonically from U to $14U/9$ as k increases.

By contrast, the dispersion relations for the anticipated vorticity method, the incompressible anticipated velocity method, and the explicit version of the PSM equation are all

$$\sigma = -\mathrm{i}kU - \nu(k^2 + l^2) - \frac{5}{72}\beta k^2 U^2, \tag{6.2}$$

provided the parameter $\lambda = 5\beta/72$ is used in the anticipated vorticity and velocity methods. The imaginary part, corresponding to the propagation speed, is unchanged from the Euler equations. There is an apparent extra anisotropic viscosity of magnitude $(5\beta/72)U^2$ in the direction of the background flow. The decay rate thus increases in proportion to k^2 without limit.

The behaviour of the two dispersion relations is plotted in figures 2 and 3 for the parameters $\beta = 0.1$, $U = 1$, and $\nu = 10^{-4}$. Since the dimensional value of $|\boldsymbol{u}|$ was absorbed into Ha and N earlier, we may take $U = 1$ without loss of generality. The value $\beta = 0.1$ is much larger than in typical laboratory applications, as $\beta = 10^{-4}$ for the parameters in the Introduction, but was chosen to illustrate the saturation of the decay rate for large wavenumbers. For these parameters saturation occurs at wavenumbers that are not so large as to prevent a comparison of the theoretical dispersion relation (6.1) with the numerical experiments reported in §8.1 below.

The two dispersion relations (6.1) and (6.2) only begin to differ significantly when the second term in the denominators of (6.1) becomes $O(1)$, or when $k \sim 8/\beta$. More
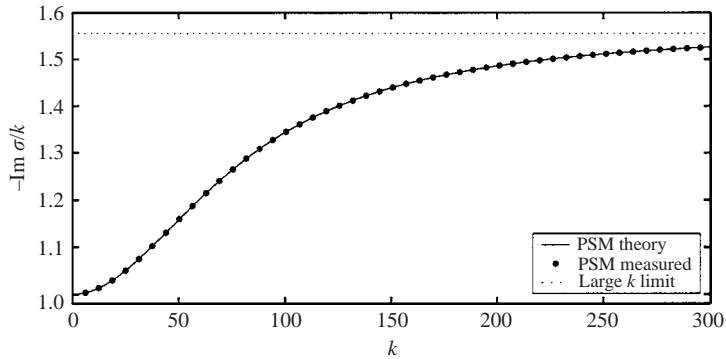
FIGURE 3. Phase speed $-\operatorname{Im}\sigma/k$ versus wavenumber k for the PSM model with $U=1$, $\beta=0.1$, and $\nu=10^{-4}$. The solid line is the theoretical prediction from equation (6.1), and the dots are numerical measurements from simulations (see §8.1). The upper dotted line is the large-wavenumber limit, $-\operatorname{Im}\sigma/k \to (14/9)U$ as $k \to \infty$. The phase speed remains unchanged for all the explicit methods.

concretely, the maximum in the group velocity is attained when the dimensionless horizontal wavenumber is

$$k = \frac{8\sqrt{3}}{\beta U} = 8\sqrt{3}\frac{NHa}{n\delta} \sim 1.4 \times 10^5, \qquad (6.3)$$

using the parameters from the Introduction. Based on these calculations, the replacement of the original PSM equation, with dispersion relation (6.1), by the explicit version with dispersion relation (6.2) is amply justified since the two only differ at very short horizontal lengthscales $k \gg \delta^{-1}N^{1/3}$. Such short lengthscales are far beyond the validity of the PSM model as a small-aspect-ratio approximation, since quasi-two-dimensionality is only valid on horizontal lengthscales larger than $aN^{-1/3}$ (Sommeria 1988). Since $N = 7.8$ for the typical parameters in the Introduction, the factors of $N^{1/3}$ make little difference to the straightforward geometrical argument that a small-aspect-ratio, or shallow-layer, approximation becomes invalid at horizontal lengthscales comparable to the layer depth.

7. Numerical method

As discussed in the Introduction, the PSM equation (1.8) is an implicit evolution equation. It contains mixed spatio-temporal derivatives arising from the $\partial_t[\psi,\omega]$ term. We rewrite equation (1.8) as

$$\omega_t - \tfrac{1}{8}\beta\{[\psi_t,\omega] + [\psi,\omega_t]\}$$
$$= -[\psi,\omega] + \nu\nabla^2\omega + \tfrac{7}{36}\beta\{[\psi,[\psi,\omega]] + [\psi_y,\omega\psi_x] + [\omega\psi_y,\psi_x]\}, \quad (7.1)$$

after neglecting the algebraic forcing and drag terms. The terms involving time derivatives have all been collected on to the left-hand side of (7.1). Even after spatial discretization, in this case using truncated Fourier series to replace $\omega(\mathbf{x},t)$ by a finite set $\{\omega_n(t)\}$, equation (7.1) cannot be written as a system of ordinary differential equations,

$$\omega_t = F(\omega), \qquad (7.2)$$

due to the terms like $[\psi, \omega_t]$ on the left-hand side. Instead, equation (7.1) is of the more general form

$$G(\omega, \omega_t) = 0, \tag{7.3}$$

that constitutes an autonomous system of differential-algebraic equations or DAEs (Brenan, Campbell & Petzold 1995; Gresho & Sani 2000). In fact, equation (7.1) takes the more restrictive form

$$\boldsymbol{M}(\omega)\omega_t = F(\omega), \tag{7.4}$$

of an implicit system of ordinary differential equations (ODEs), since the left-hand side of equation (7.1) may be written as an invertible linear operator $\boldsymbol{M}$ acting on ω_t. A genuine differential-algebraic system only arises when $\boldsymbol{M}(\omega)$ may be singular, but since good algorithms are available to solve the more general form equation (7.3) (Brenan *et al.* 1995), there seemed little need to exploit this special case.

Most algorithms for DAEs are quite similar to implicit multistep methods for solving systems of ODEs. As a simple example, consider applying the backwards Euler method, in which ω_t is approximated by the first-order finite difference formula $h^{-1}(\omega^{(t+h)} - \omega^{(t)})$ for a timestep of length h, and ω is replaced by its value $\omega^{(t+h)}$ at the end of the timestep. Equations (7.2) and (7.3) then become

$$h^{-1}\big(\omega^{(t+h)} - \omega^{(t)}\big) = F\big(\omega^{(t+h)}\big), \tag{7.5a}$$

$$G\big(\omega^{(t+h)}, h^{-1}(\omega^{(t+h)} - \omega^{(t)})\big) = 0. \tag{7.5b}$$

Both equations have become nonlinear algebraic systems for $\omega^{(t+h)}$, which may be solved by Newton's method. In practical implementations the crude first-order approximation $\partial_t \omega = h^{-1}(\omega^{(t+h)} - \omega^{(t)}) + O(h)$ is replaced by higher-order formulae involving $\omega^{(t-h)}$ and earlier values.

The numerical experiments were performed using the freely available DAE solver package DASPK (Brown, Hindmarsh & Petzold 1994), the successor to the (also freely available) DASSL (Petzold 1983). DASPK improves upon its predecessor by solving the linear systems of equations that arise within Newton's method using preconditioned Krylov space (PK) methods (e.g. Saad 1996; Trefethen & Bau 1997) instead of the direct $\boldsymbol{LU}$ factorization approach of DASSL. This improvement allows much larger ODE systems to be tackled. In the direct approach used by DASSL, linear systems of the form $\boldsymbol{Ax} = \boldsymbol{b}$ that arise from Newton's method are solved by factorizing the matrix as $\boldsymbol{A} = \boldsymbol{LU}$, where $\boldsymbol{L}$ and $\boldsymbol{U}$ are lower and upper triangular matrices respectively. In other words, all entries of $\boldsymbol{L}$ vanish strictly above the diagonal, and all entries of $\boldsymbol{U}$ vanish strictly below the diagonal. Solving the linear system $\boldsymbol{Ax} = \boldsymbol{b}$ then reduces to solving the lower triangular system $\boldsymbol{Ly} = \boldsymbol{b}$ by forward substitution, and the upper triangular system $\boldsymbol{Ux} = \boldsymbol{y}$ by back substitution (Golub & Van Loan 1996; Trefethen & Bau 1997).

Unfortunately, the matrices $\boldsymbol{A}$, $\boldsymbol{L}$, and $\boldsymbol{U}$ arising in the 256×256 resolution computations presented below each contain $256^4 \approx 4 \times 10^9$ entries, and would consume a prohibitive 32 gigabytes of storage. However, the preconditioned Krylov space methods mentioned above are able to solve linear systems of the form $\boldsymbol{Ax} = \boldsymbol{b}$ without computing or storing the matrix $\boldsymbol{A}$. Instead, only matrix-vector products, i.e. $\boldsymbol{Ax}$ for general $\boldsymbol{x}$, need be computed. Krylov space methods are iterative, computing successively better approximations to the exact solution until they reach some stopping criterion. These approximations are all of the form $\boldsymbol{x} \approx P_n(\boldsymbol{A})\boldsymbol{b}$, where successive polynomials P_n of degree $n = 1, 2, 3, \ldots$ are typically constructed so that the difference between the approximate solution $P_n(\boldsymbol{A})\boldsymbol{b}$ and the true solution $\boldsymbol{x}$ is minimal

in some norm. In particular, DASPK uses the generalized minimal residual algorithm (GMRES) devised by Saad & Schultz (1985) for solving general non-symmetric linear systems. For each n, GMRES minimizes the ℓ_2 norm of the residual $||\mathbf{A}P_n(\mathbf{A})\mathbf{b} - \mathbf{b}||_2$ over all polynomials of degree n.

7.1. *Preconditioning*

Krylov space methods typically benefit from preconditioning, the replacement of the original linear system $\mathbf{A}\mathbf{x} = \mathbf{b}$ by the equivalent system $\mathbf{P}^{-1}\mathbf{A}\,\mathbf{x} = \mathbf{P}^{-1}\mathbf{b}$. The matrix $\mathbf{P}$ is called the preconditioner (e.g. Saad 1996; Golub & Van Loan 1996; Trefethen & Bau 1997), and should be chosen to approximate $\mathbf{A}$, subject to the constraint that $\mathbf{P}^{-1}\mathbf{x}$ be relatively easy to compute for any $\mathbf{x}$. The numerical experiments reported below employed a simple preconditioner based on the operator $h^{-1} - \nu\nabla^2$ arising from just the $\partial_t\omega$ and $\nu\nabla^2\omega$ terms in equation (7.1). This preconditioning matrix becomes diagonal, $h^{-1} + \nu k^2$, in Fourier space, and so may be inverted very simply. With this preconditioner, the GMRES solver converged in around fifteen iterations for all sizes of problem considered, ranging from 64×64 to 512×512 Fourier modes. The linear systems are most ill-conditioned during the computation of consistent initial conditions (see below), and the average number of GMRES iterations necessary during the time integrations of a turbulent flow reported below turned out to be even smaller, only three or four. Some concrete figures are given in tables 1 and 2 in §9.

7.2. *Nonlinear terms*

The nonlinear terms were evaluated pseudo-spectrally, i.e. using a collocation approach. More precisely, the DAE integrator was applied to gridpoint values of ω and ω_t in physical space, and products were computed in physical space, while spatial derivatives were computed spectrally. Gridpoint values were used because the adaptive error and stepsize control in the DAE integrator works much better for systems of equations in which the variables are all of the same order of magnitude. Thus if the DAE integrator were applied to the Fourier coefficients instead of the gridpoint values, it would be necessary to estimate the exponent γ of the spectrum $\omega_{\mathbf{k}} \propto |\mathbf{k}|^{-\gamma}$ in order to rescale the $\omega_{\mathbf{k}}$ to be the same order of magnitude for all wavevectors $\mathbf{k}$. No de-aliasing procedure was used, on the grounds that the simulations were sufficiently well resolved to render de-aliasing redundant. The fast Fourier transforms between physical and spectral space were computed using the library FFTW version 2.1.3 by Frigo & Johnson (1998).

7.3. *Initial conditions*

The computation of consistent initial conditions, in this case ω and ω_t that together satisfy equation (7.1), is often problematic for DAE systems (Brown, Hindmarsh & Petzold 1998), because Newton's method may not converge without a good first approximation. In the computations presented below, equation (7.1) was first solved crudely for ω_t given ω by fixed point iteration, i.e. by first setting ω_t equal to the right-hand side, using this first approximation in the $[\psi_t, \omega] = [\nabla^{-2}\omega_t, \omega]$ and $[\psi, \omega_t]$ terms, and iterating. The successive iterates did not converge to an exact solution in general, because the relevant operator on the left-hand side of equation (7.1) is not a contraction, so the iterations were halted when the ℓ_2 norm of the residual stopped decreasing. This procedure provided an adequate initial guess for the initialization routine in DASPK to compute a consistent ω_t from ω. Alternatively, equation (7.1) could have been solved directly as a linear system of equations for ω_t using Krylov space methods, but the approach described above using fixed point iteration was easier to implement and worked well enough.

7.4. *Explicit ODE systems*

In contrast to the implicit PSM equation, the comparison models in equations (1.10) and (1.14), and the explicit version of the PSM equation in (2.13), all give explicit expressions for $\partial_t \omega$. While it is simplest to solve them using the same DAE integrator used for equation (7.1) as described above, it proved slightly faster to use the conventional ODE integrator VODPK. This integrator is a modification of the earlier VODE (variable coefficient ODE) solver by Brown, Byrne & Hindmarsh (1989) to use preconditioned Krylov (PK) methods. For these ODE systems the fully explicit Adams–Bashforth integration method in VODPK worked well enough, because the main constraint on the timestep was the accuracy of the advection rather than the accuracy or stability of the diffusion.

To be concrete, the three explicit equations solved along with the original PSM equation without forcing or drag in the form (7.1) are the explicit PSM equation without forcing or drag,

$$\partial_t \omega + [\psi, \omega] = \nu \nabla^2 \omega - \tfrac{1}{8}\beta[\nabla^{-2}[\psi, \omega], \omega] + \tfrac{5}{72}\beta[\psi, [\psi, \omega]] + \tfrac{7}{36}\beta\{[\psi_y, \omega\psi_x] + [\omega\psi_y, \psi_x]\}, \tag{7.6}$$

the viscous anticipated vorticity method

$$\partial_t \omega + [\psi, \omega] = \nu \nabla^2 \omega + \lambda[\psi, [\psi, \omega]], \tag{7.7}$$

and the viscous anticipated velocity method

$$\partial_t \omega + [\psi, \omega] = \nu \nabla^2 \omega + \lambda\{[\psi, [\psi, \omega]] + [\psi_y, \omega\psi_x] + [\omega\psi_y, \psi_x] + 2\nabla \cdot ([\psi_y, \psi_x] \nabla\psi)\}. \tag{7.8}$$

All four equations were solved with the same value for the viscosity ν, and with the parameters λ and β related by $\beta = (72/5)\lambda$ so that the coefficients of the $[\psi, [\psi, \omega]]$ term are all equal in all four equations. Some isotropic diffusion ($\nu > 0$) proved necessary for numerical stability, even though the λ and β terms provide a form of dissipation even when $\nu = 0$.

8. Roll-up of shear layers

Minion & Brown (1997) studied the performance of various numerical schemes in under-resolved simulations of the two-dimensional incompressible Navier–Stokes equations. Their initial conditions corresponded to a pair of perturbed shear layers,

$$u_x = \begin{cases} \tanh(\kappa(y - 1/4)), & y \leqslant 1/2, \\ \tanh(\kappa(3/4 - y)), & y > 1/2, \end{cases}$$
$$u_y = \epsilon \sin(2\pi(x + 1/4)),$$

in the doubly periodic domain $0 \leqslant x, y \leqslant 1$. The parameter κ controls the width of the shear layers, and ϵ the magnitude of the initial perturbation. The shear layers roll up due to a Kelvin–Helmholtz instability excited by the $O(\epsilon)$ perturbation in u_y. These initial conditions may be thought of as representing a small portion of the electrically forced circular shear layer in the MATUR experiment (Alboussière *et al.* 1999; Messadek & Moreau 2002).

8.1. *Linear waves*

The numerical method described in §7 assumes that the vorticity ω and streamfunction ψ may both be expanded as Fourier series. This assumption therefore excludes

simulation of a uniform stream in the x-direction, say, because $\psi = Uy$ is not periodic even though u, v, and ω are all periodic. In principle the numerical method could be modified to add a constant U wherever ψ_y appears in equation (1.10), since ψ itself never appears undifferentiated after the Jacobians $[\cdot, \cdot]$ have been expanded, but such extensive modifications would rather spoil the purpose of the experiments for validating the original numerical implementation.

However, the unperturbed initial conditions in equation (8.1) comprise two oppositely directed uniform streams separated by thin shear layers, and this flow can be represented by a doubly periodic streamfunction. For sufficiently short times, the vorticity disturbance proportional to ϵ behaves as though it were a perturbation to a uniform stream. Although the perturbation excites Kelvin–Helmholtz instabilities of the shear layers that eventually grow to obliterate the original vorticity wave, as described below, for a short time the disturbance created by these instabilities remains negligible near the centreline.

The amplitude and phase of the disturbance were computed from the one-dimensional Fourier representation of the vorticity on the centreline $y = 1/2$ between the two shear layers. Least-squares linear fits to the phase and logarithm of the amplitude as functions of time t for $0 \leqslant t \leqslant 0.01$ yielded an experimental phase speed and decay rate. The agreement between the experiments and the theoretical predictions from equation (6.1) was found to be excellent, as shown in figures 2 and 3. The correct theoretical decay rates were typically recovered to four significant figures, and the correct phase speeds to five or more significant figures.

8.2. *Nonlinear development*

Figures 4 and 5 show the evolution of the vorticity, starting from the two horizontal shear layers given in equation (8.1) with $\epsilon = 0.05$ and $\kappa = 40$ under the Navier–Stokes equations, the anticipated vorticity method, the anticipated velocity method, and the PSM model without linear drag. All four numerical experiments were performed on a 256×256 grid, and all four equations included a Navier–Stokes viscous term corresponding to an initial Reynolds number $Re = 2 \times 10^4$ based on the maximum velocity and the domain size. Some isotropic viscosity is necessary in all four equations for numerical stability. The PSM parameter $\beta = (72/5)\lambda = 0.0576$ was chosen so that the dispersion relation (6.1) matches the dispersion relation for the anticipated vorticity and velocity methods at leading order. The numerical solutions shown here were validated by comparing the solution for the anticipated velocity method with independent solutions of the compressible analogue of the anticipated velocity method obtained using a lattice Boltzmann formulation (Dellar 2004). These lattice Boltzmann solutions converged to solutions obtained using the spectral method described above with the expected $O(Ma^2)$ compressibility error, and $O(N_x^{-2})$ spatial truncation error on an $N_x \times N_x$ grid. Detailed convergence graphs may be found in Dellar (2004).

Figures 4(a) and 5(a), for the unmodified Navier–Stokes equations, show the shear layers winding up into two spiral vortices, which is the expected nonlinear development of the Kelvin–Helmholtz instability initiated by the perturbation u_y in the initial conditions. The anticipated vorticity method, equation (1.10) with parameter $\lambda = 0.004$, as shown in Figures 4(b) and 5(b), leaves the location of the wound-up shear layers unaffected, but containing noticeably less intense vorticity. The peak vorticity, located in the centres of the two vortices, is almost unchanged, and remains substantially greater in magnitude than the vorticity in the filaments around each vortex. The vortices in the anticipated vorticity method are noticeably more axisymmetric, especially at the later time $t = 1.2$ in figure 5, than in the Navier–Stokes equations.
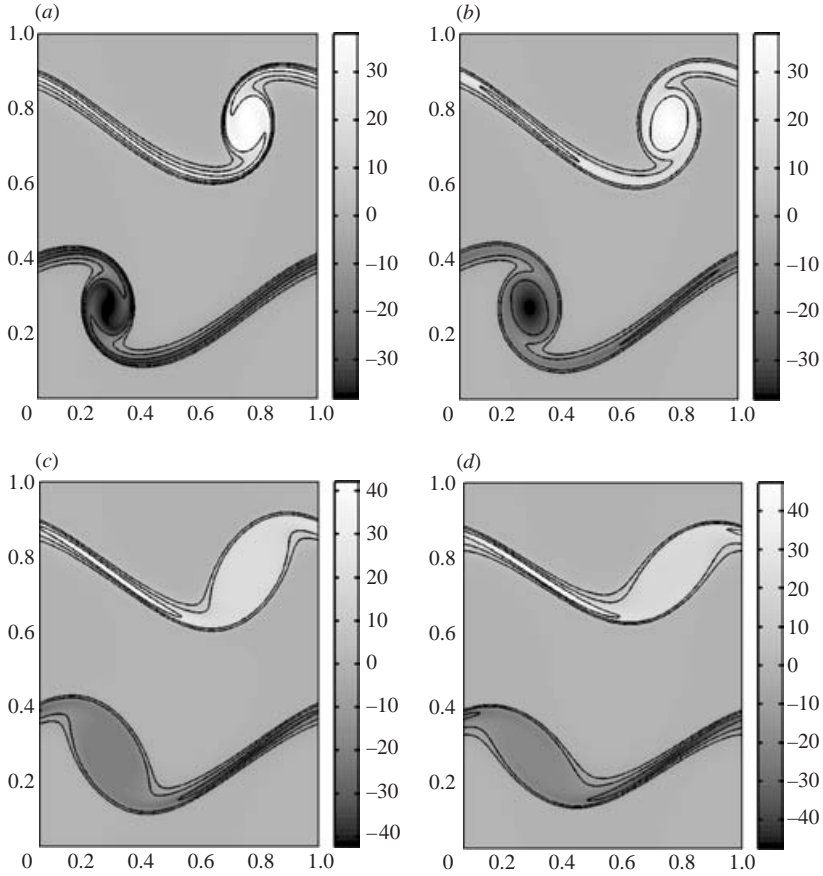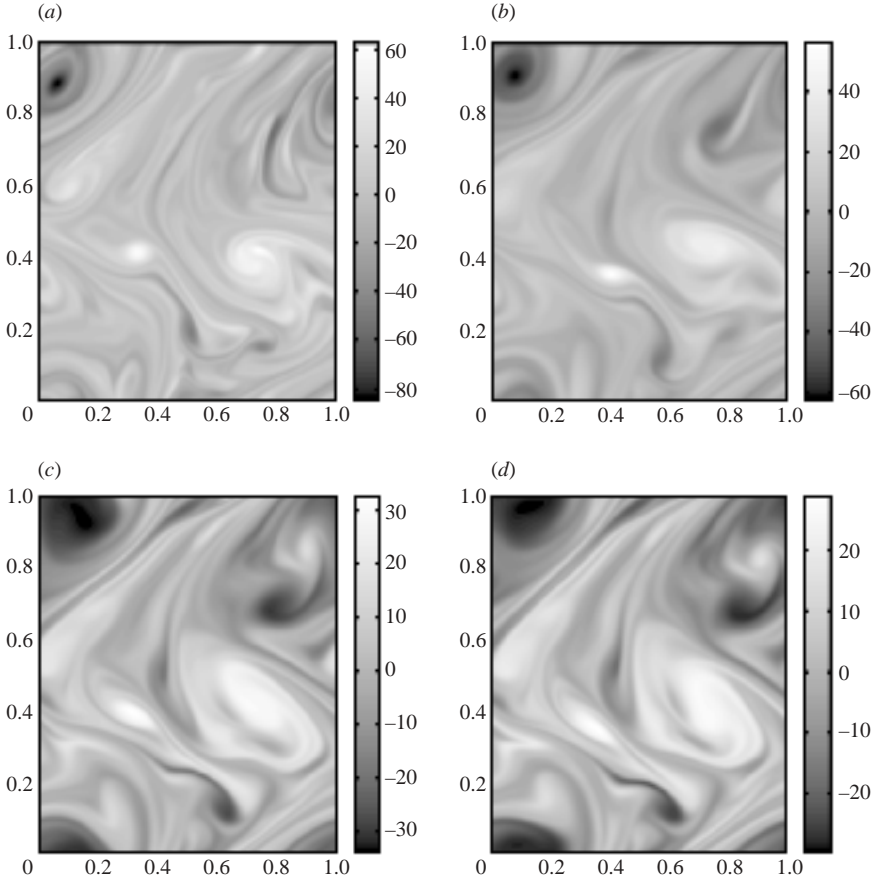
FIGURE 4. The vorticity at time $t = 0.80$ from (*a*) the unmodified Navier–Stokes equations, (*b*) the anticipated vorticity method with $\lambda = 0.004$, (*c*) the anticipated velocity method also with $\lambda = 0.004$, and (*d*) the PSM model with $\beta = (72/5)\lambda = 0.0576$. All four equations included a linear viscous term corresponding to an initial Reynolds number of 2×10^4.

This is what one would expect from the $[\psi, [\psi, \omega]]$ term in the anticipated vorticity method diffusing vorticity along the (roughly circular) streamlines in the vortices.

By contrast, the anticipated velocity method (also with $\lambda = 0.004$) and the PSM equation, as shown in plots (*c*) and (*d*) respectively, both lead to two larger homogenized elliptical patches of uniform vorticity instead of the spiral vortices. This behaviour may be attributed to the $[\psi_y, \omega\psi_x] + [\omega\psi_y, \psi_x]$ terms present in both equations. These are the terms responsible for the outward spreading of vorticity in axisymmetric flows, as expressed by the $(\Gamma^3)_s$ term in the circulation form (2.11) of the PSM equation. This effect is due to Ekman pumping driven by radial pressure gradients transporting vorticity outwards, as explained in §2. Any curvature of the streamlines requires a pressure gradient to balance the centrifugal force, so it is reasonable to expect that the Ekman pumping would cause curved streamlines to move outwards in non-axisymmetric flows as well.

Finally, the tilted elliptical form of the vortices may be attributed to the diffusion of vorticity along the streamlines inside the shear layers into the vortices. This has the effect of feeding in vorticity at the two attachment points where the shear layers merge with the edge of the vortices. The location of the peak vorticity has also moved
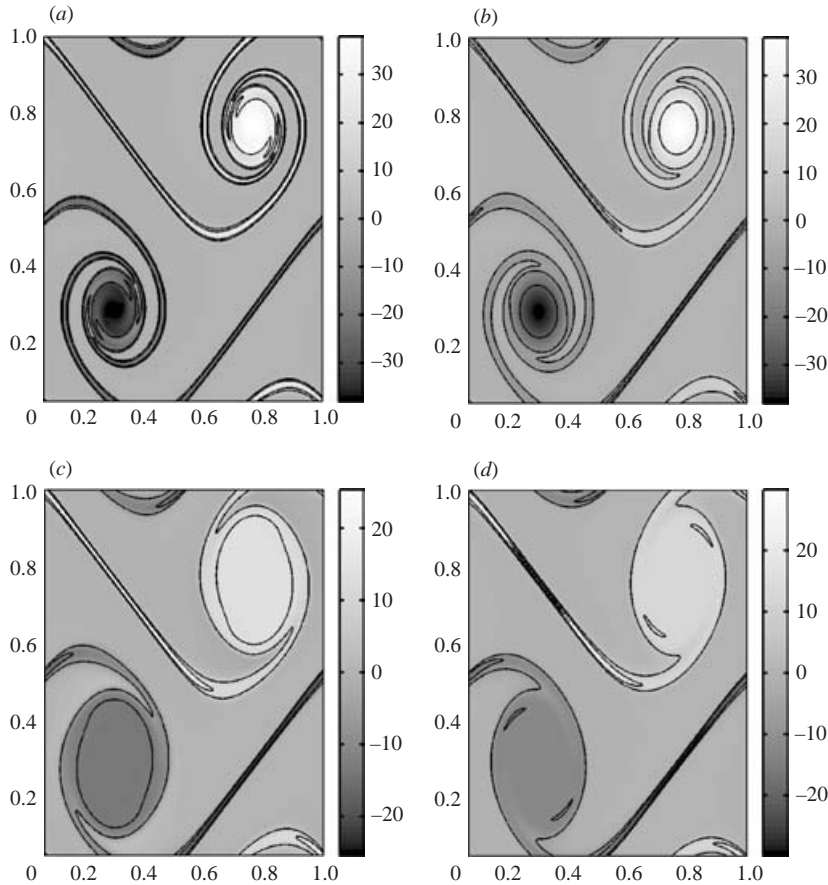
FIGURE 5. The vorticity at the later time $t = 1.2$ from the same four sets of equations as figure 4.

from the centres of the vortices to the middle of the shear layers, more noticeably in the PSM equation, since the expansion of the elliptical vortices is accompanied by a corresponding reduction in the value of the vorticity in order to conserve circulation.

9. Freely decaying turbulence

The previous figures show the effect of the various extra terms in the anticipated vorticity, anticipated velocity, and PSM equations on the formation of a pair of coherent vortices from simple initial conditions. In this section we consider the evolution of more complex initial conditions, a k^{-3} energy spectrum with uniformly distributed random phases. This energy spectrum is normally taken to signify a forwards enstrophy cascade to small scales (Kraichnan 1967; Batchelor 1969), but in liquid-metal experiments it may also be attributed to the usual inverse energy cascade being modified by Hartmann braking (Messadek & Moreau 2002) because the algebraic drag $-n\alpha\overline{\boldsymbol{u}}/t_{\mathrm{H}}$ from Hartmann braking provides dissipation at all wavenumbers, as discussed in the Introduction.

The initial conditions were scaled to have unit kinetic energy. With this normalization, the initial peak vorticity $\omega_{\mathrm{max}} \gtrsim 130$ was much larger than in the

FIGURE 6. The vorticity at $t = 1.0$ from (*a*) the unmodified Navier–Stokes equations, (*b*) the anticipated vorticity method with $\lambda = 4 \times 10^{-4}$, (*c*) the anticipated vorticity method also with $\lambda = 4 \times 10^{-4}$, and (*d*) the PSM model with $\beta = (72/5)\lambda = 0.00576$. All four equations included a linear viscous term corresponding to an initial Reynolds number of 10^4.

previous experiments, so the parameters $\lambda = 4 \times 10^{-4}$ and $\beta = (72/5)\lambda \approx 0.0058$ in front of the cubic nonlinear terms were chosen to be correspondingly smaller. The simulations shown were performed on a 256×256 grid. Each equation included an isotropic Navier–Stokes viscous term with $\nu = 10^{-4}$, corresponding to a Reynolds number $Re = 10^4$ based on the initial kinetic energy and domain size. These parameters are reasonably indicative of laboratory experiments, although the parameters λ and β multiplying the linear and nonlinear diffusion terms are both too large. True laboratory values would require both a finer computational grid, and the simulation of many more eddy turnover times.

Figure 6 shows the vorticity field at time $t = 1.0$ that evolved from one realization of these random initial conditions under the four different equations. While it is difficult to make a direct comparison because various features are shifted slightly between plots (*c*) and (*d*), so that a pointwise correlation is not very useful, it should be apparent that plots (*c*) and (*d*) resemble each other more closely than any other pair. A second noticeable feature is that plots (*c*) and (*d*) show much larger areas covered by regions of close-to-extremal vorticity, areas of very light or very dark shading.
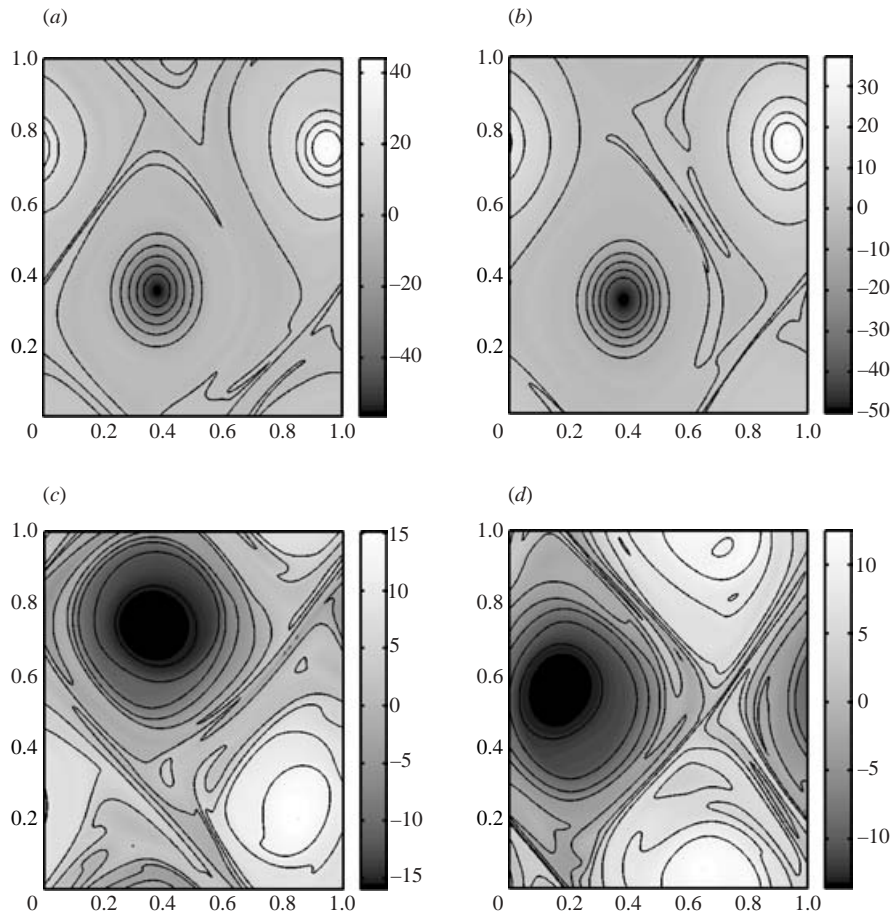
FIGURE 7. The vorticity at the later time $t = 5.0$ for the same four equations and parameter values as figure 6.

These comparisons are reinforced by the vorticity fields at the later time $t = 5.0$ shown in figure 7. The initial conditions have now evolved into vortex dipoles under all four different equations. The Navier–Stokes and anticipated vorticity method solutions, which are very similar, comprise two fairly small but intense isolated vortices in a background of very weak vorticity. By contrast, the vortices in the PSM and anticipated velocity method solutions, which are again qualitatively very similar, have much weaker peak vorticities, but the two vortices in each solution have expanded to fill the computational domain.

These visual impressions may be quantified by plotting the evolution of the kurtosis, or flatness, of the vorticity field. McWilliams (1984) and Weiss & McWilliams (1993) used the kurtosis, defined by

$$\mathcal{K} = \mathcal{L}^{-2} \frac{1}{4} \int \omega^4 \, \mathrm{d}x \, \mathrm{d}y = \frac{\langle \omega^4 \rangle}{\langle \omega^2 \rangle^2}, \tag{9.1}$$

as a measure of intermittency, and thus of the formation of coherent structures. The evolution of the kurtosis turns out to be more illuminating than the evolution of the energy $\langle \frac{1}{2} u^2 \rangle$, the enstrophy $\langle \frac{1}{2} \omega^2 \rangle$, or the palinstrophy $\langle |\nabla \omega|^2 \rangle$, all of which will
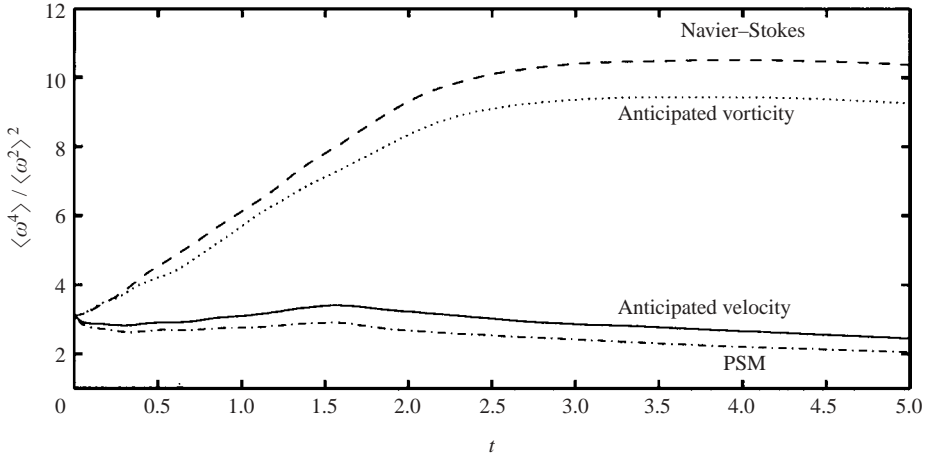
FIGURE 8. Evolution of the kurtosis $\langle\omega^4\rangle/\langle\omega^2\rangle^2$ for the same four equations and parameter values as figure 6.

be discussed later. Moreover, the energy spectra of the vorticity fields at $t = 1.0$ for the three modified equations are almost indistinguishable from each other. Spectra are not very useful for investigating coherent structure formation because the crucial phase information is lost.

The reciprocal $\mathcal{K}^{-1}$ of the kurtosis reflects the fraction of the area occupied by the dominant structures in ω. The kurtosis is thus expected to be $O(R^2/r^2)$ for a flow field comprising isolated coherent structures of lengthscale r, separated by a larger typical mean distance R (McWilliams 1984). By contrast, a uniform vorticity field with $\omega = \text{const}$ has kurtosis $\mathcal{K} = 1$. The kurtosis of the vorticity field, given by (9.1), should not be confused with the kurtosis of various probability density functions reported by Sommeria (1988) based on correlations between low-order modes and the value of the streamfunction at one point.

Figure 8 shows the evolution of the kurtosis for the same four different equations with the same random initial conditions. Being the superposition of many independent random phases, the initial conditions approximate a Gaussian random variable, and therefore have kurtosis $\mathcal{K} = 3$. The kurtosis increases initially for the Navier–Stokes equations and anticipated vorticity method, due to the formation of isolated coherent vortices by the inverse cascade. The time interval $2.0 < t < 2.5$ in which the growth in kurtosis saturates marks the final reduction of the number of vorticity extrema down to two through vortex merging. The kurtosis subsequently decays gradually due to slow viscous spreading of the remaining two vortices.

By contrast, the spreading of vorticity extrema under the PSM and anticipated velocity equations causes the kurtosis to decrease slightly from the initial conditions. Although comparatively extended regions of large positive or negative vorticity form for these two equations, as shown in figures 6(*c*) and 6(*d*), they are not isolated by surrounding quiescent regions of weak vorticity, and so do not contribute to an increase in the kurtosis. The qualitative behaviour, as seen in both the vorticity fields and the kurtosis, resembles that found by Polvani *et al.* (1994) in their study of two-dimensional turbulence in the rotating-shallow-water equations. The rotation rate Ω and finite surface gravity wave speed $\sqrt{gh}$ define a lengthscale $L_D = \sqrt{gh}/\Omega$ called the deformation radius. On scales much smaller than L_D, solutions of the rotating-shallow-water equations behave like incompressible two-dimensional flows, so Polvani
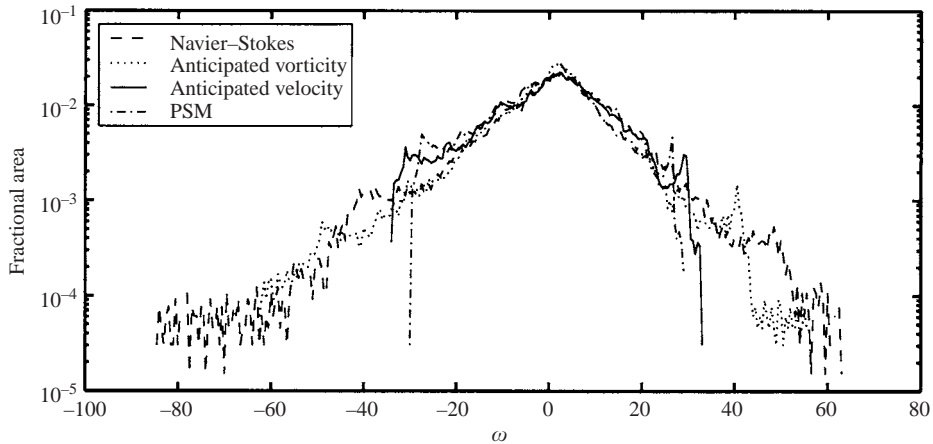
FIGURE 9. Histogram of vorticity values at $t = 1.0$ for the same four equations and parameter values as figure 6.

et al. (1994) found the expected growth in kurtosis over time indicating the formation of isolated coherent structures. The background rotation becomes important on scales comparable to L_D, which sets a natural maximum scale for vortices. Vortices on the scale of L_D evolve very slowly, and Polvani *et al.* (1994) found large areas covered by patches of extremal vorticity, with a kurtosis comparable to their (also Gaussian) initial conditions. The difference between this shallow-water system and the PSM or anticipated velocity method is that the latter have no maximum size for vortices analogous to L_D, so the vortices continue growing until they fill the domain.

More quantitatively, the kurtosis may also be interpreted as measuring the tails of the vorticity distribution. Figure 9 shows histograms of the vorticity at $t = 1.0$ at the 256^2 collocation points, with a binning interval $\Delta\omega$ of 0.5, from the numerical simulations of the four different evolution equations. These histograms serve as approximations to the vorticity probability density functions (PDFs) that would arise from an ensemble of random initial conditions. By time $t = 1.0$ the Gaussian initial conditions, which would appear as a parabola on these semi-logarithmic axes, have evolved under all four equations into the characteristic double exponential form of two straight lines meeting at $\omega = 0$. However, the histograms for the anticipated velocity method and the PSM equation cut off sharply, whereas the tails for the Navier–Stokes and anticipated vorticity method extend much further out, albeit with very small densities. In the second set of histograms at the later time $t = 5.0$ shown in figure 10, the Navier–Stokes and anticipated vorticity method solutions both have exponentially decaying tails extending out to extreme values of the vorticity, while the PSM and anticipated velocity method both produce sharp cutoffs. Moreover, the vorticity distribution is peaked at or very near the cutoffs, as one would expected from the hyperbolic behaviour of axisymmetric solutions described in § 2.

Figures 11 to 13 show the evolution of more conventional quantities, the energy $\langle \frac{1}{2}u^2 \rangle$, enstrophy $\langle \frac{1}{2}\omega^2 \rangle$, and palinstrophy $\langle |\nabla\omega|^2 \rangle$, under the four different equations. Figures 12 and 13 for the enstrophy and palinstrophy use a logarithmic scale on the vertical axis in order to show the evolution more clearly. Energy decay in both the Navier–Stokes equations and the anticipated vorticity method is purely viscous, and at a rate proportional to the enstrophy. The energy in fact decays more slowly under the anticipated vorticity method, because the additional $[\psi, [\psi, \omega]]$ term reduces the
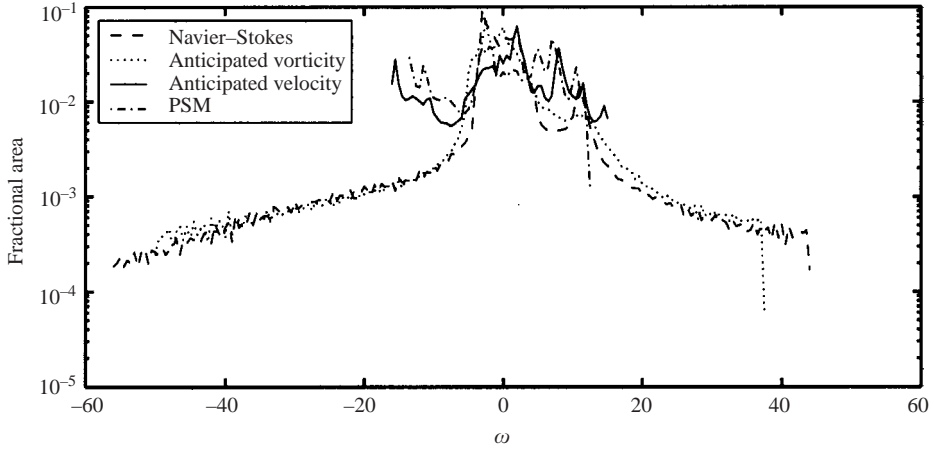
FIGURE 10. Histogram of vorticity values at $t = 5.0$ for the same four equations
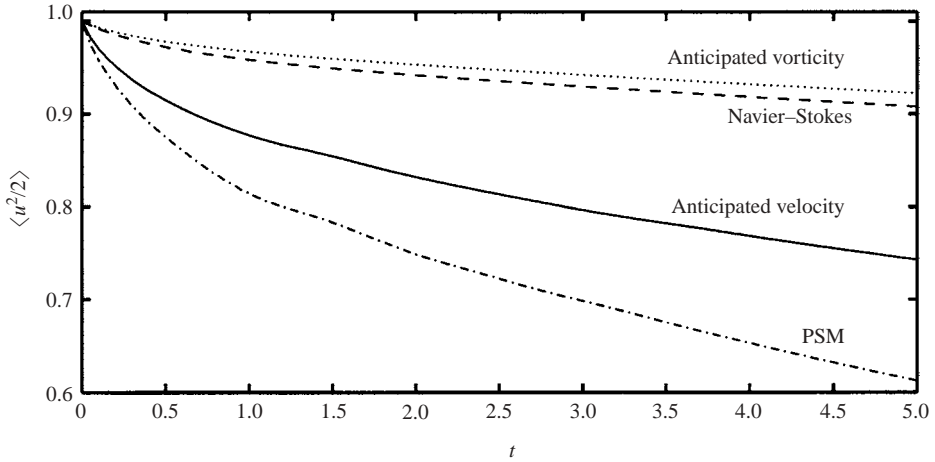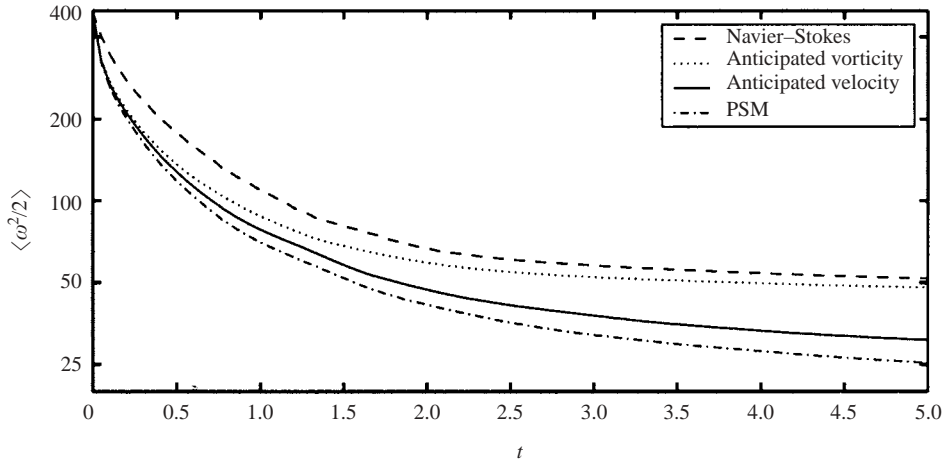and parameter values as figure 6.

FIGURE 11. Evolution of the energy $\langle \frac{1}{2}u^2 \rangle$ for the same four equations and parameter
values as figure 6.

enstrophy, and hence the energy decay rate, but does not affect the energy directly.
By contrast, the additional terms $[\psi_y, \omega\psi_x]$ and $[\omega\psi_y, \psi_x]$ in the anticipated velocity
method and the PSM equation dissipate energy directly, even in the absence of
viscosity, as shown in (5.8).

The relation $\lambda = (5/72)\beta$ between the parameters in the anticipated vorticity/velocity
methods and the PSM equation was chosen to make the decay rates of linear waves
equal, according to the analysis in §6. Although there is no simple expression for
the energy dissipation rate in the PSM equation, due to the $\partial_t[\psi, \omega]$ term, equation
(5.6) gives upper and lower bounds for the energy dissipation rate in the explicit
version of the PSM equation in terms of the integrals of ω^2 and $|\mathbf{u} \cdot \nabla \mathbf{u}|^2$. The relation
$\lambda = (5/72)\beta$ also makes the lower bound for the energy decay rate in the PSM equation
in (5.6) coincide with the energy decay rate for the anticipated velocity method given
in (5.8). Figure 11 shows that the energy in fact decays more quickly in the PSM

FIGURE 12. Evolution of the enstrophy $\langle \frac{1}{2}\omega^2 \rangle$ on a logarithmic scale for the same four equations and parameter values as figure 6.
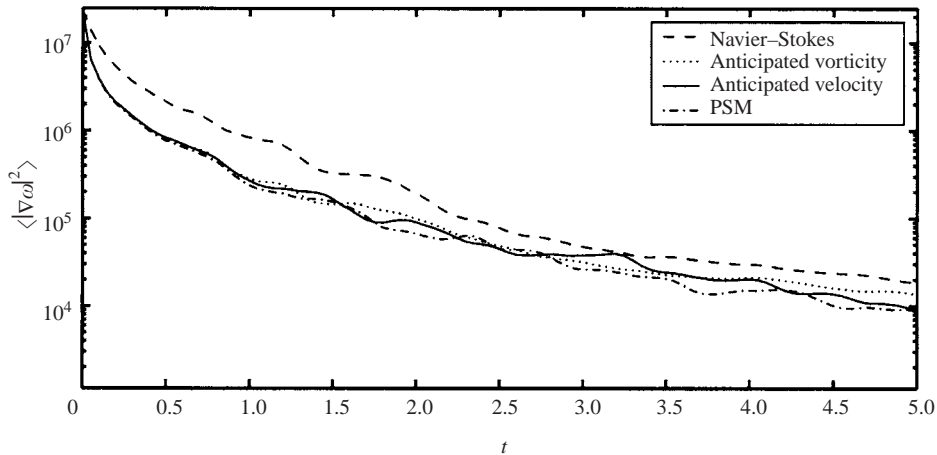
FIGURE 13. Evolution of the palinstrophy $\langle |\nabla \omega|^2 \rangle$ on a logarithmic scale for the same four equations and parameter values as figure 6.

equation than in the anticipated velocity method with the same initial conditions, but it is not surprising that the energy decay rate lies above, rather than precisely on, the calculated lower bound.

When the energy dissipation is primarily inviscid, through the $|\boldsymbol{u} \cdot \nabla \boldsymbol{u}|^2$ term rather than the ω^2 term, as in these numerical experiments, the upper bound in equation (5.6) is $14/5 = 2.8$ times the lower bound. Figure 14 shows the ratio of the true energy decay rate in the PSM equation to the calculated upper and lower bounds for five different realizations of the random initial conditions described above. Initially the energy decay rate in all five realizations is about 1.3 times the lower bound, but increases over time to approach the upper bound. This suggests that the non-local $[\psi, \omega]\nabla^{-2}[\psi, \omega]$ term in the PSM energy equation (5.5) becomes successively less significant relative to the $[\psi, \psi_x]$ and $[\psi, \psi_y]$ terms as the solution evolves towards larger spatial lengthscales. A close inspection of figure 14 suggests two different
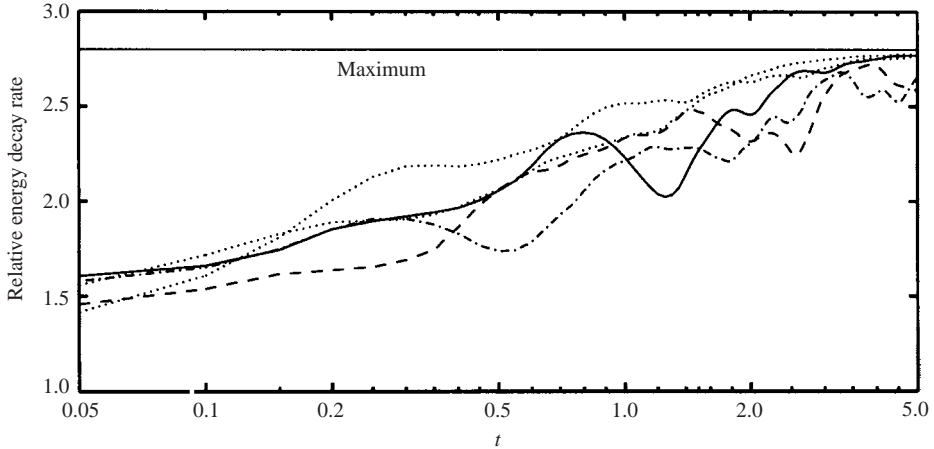
FIGURE 14. Ratio of the energy decay rate in the PSM equation to the minimum given in (5.6) for five different realizations with the same parameter $\beta = 0.00576$ and initial Reynolds number $Re = 10^4$. The upper bound becomes 2.8 times the lower bound in the inviscid limit, and is shown by the horizontal line.

outcomes at long times: three of the realizations seem to asymptote to the upper bound, while the other two oscillate distinctly below the upper bound. This is because the periodic boundary conditions allow the flow to become almost independent of one coordinate, like the initial conditions used in the previous section, as an alternative to forming the the vortex dipoles shown in figure 7. The three realizations asymptoting to the upper bound all form vortex dipoles at large times, while the remaining two form one-dimensional flows.

Figure 12 shows the evolution of the enstrophy under the Navier–Stokes equations, and under the three different modified equations. The vertical axis uses a logarithmic scale to clarify the behaviour at later times when the enstrophy is only a tenth its initial value. The three modified equations show very similar behaviour initially, but then diverge. This is probably because the initial conditions contain comparatively large high-wavenumber contributions to the enstrophy that are damped by the $[\psi, [\psi, \omega]]$ anticipated vorticity term that is common to all three modified equations, and is the only term containing second derivatives of the vorticity. The extra terms in the anticipated velocity and PSM equations only involve lower derivatives of the vorticity. These term eventually become significant, and then cause the enstrophy to decay more rapidly than in the anticipated vorticity method. Although the additional terms in the PSM and anticipated velocity and enstrophy equations are not sign-definite, in these numerical experiments they do have the effect of increasing the enstrophy decay rate.

Similarly, the evolution of the palinstrophy $\langle |\nabla \omega|^2 \rangle$ plotted in figure 13 under the three modified equations is very similar for $t \lesssim 1$, and remains quite similar thereafter. Again, this is probably because the palinstrophy is dominated by the high-wavenumber components of the vorticity field, and these are predominantly affected by the $[\psi, [\psi, \omega]]$ anticipated vorticity term that is common to all three modified equations.

9.1. *Relative computational expense*

The numbers in tables 1 and 2 give a rough idea of the relative computational expense of simulating the various different equations. The run times are all for a

PDE	CPU time (min)	Nonlinear iterations (timesteps)	Linear iterations	Ratio
Navier–Stokes	5.3	999	3032	3.0
anticipated vorticity method	5.1	194	2595	13.4
anticipated velocity method	10.9	217	2511	11.6
PSM explicit	8.8	194	2296	11.8
PSM implicit	76.3	1249	20482	16.4

TABLE 1. Computational work to solve the 256×256 rollup problem to $t = 1.2$.

PDE	CPU time (min)	Nonlinear iterations (timesteps)	Linear iterations	Ratio
Navier–Stokes	18	4715	9379	2.0
anticipated vorticity method	12	1781	5357	3.0
anticipated velocity method	29	1664	5597	3.4
PSM explicit	25	1625	5536	3.4
PSM implicit	72	3908	17076	4.4

TABLE 2. Computational work to solve the 256×256 turbulence problem to $t = 1.0$.

2.4 GHz Pentium 4 computer using GNU Fortran version 3.3.1, FFTW version 2.1.3 by Frigo & Johnson (1998), and DASPK version 3.0 by Li & Petzold. This version of DASPK is a more recent implementation than the version described in Brown *et al.* (1994). The relative and absolute error tolerances were both taken to be 10^{-5} in the time integration. From a comparison with solutions computed using a 10^{-7} tolerance, the vorticity was in fact computed to a true accuracy of about 3×10^{-5}. About half the computational time was consumed by the fast Fourier transforms (FFTs).

The plain Navier–Stokes equations appear relatively expensive because they retain far more fine-scale structure in the vorticity field than any other equation considered, so the time integration requires about three and a half times as many timesteps to achieve the same accuracy in the advection. The anticipated vorticity method, the anticipated velocity method, and the explicit form of the PSM equation are all very similar in terms of the number of timesteps required. The small ratio of linear to nonlinear iterations shows that the simple diagonal preconditioner based on the viscous term is very effective. The simple form of the nonlinear terms makes the anticipated vorticity method the fastest of the three in terms of CPU time, while the anticipated velocity method is the slowest, mainly because the $2\nabla \cdot ([\psi_y, \psi_x] \nabla \psi)$ term is slower to evaluate pseudospectrally than the other nonlinear terms expressed as Jacobians. The original PSM equation with its implicit $\partial_t (\boldsymbol{u} \cdot \nabla \boldsymbol{u})$ or $\partial_t [\psi, \omega]$ term is substantially slower than the explicit version (2.13) that eliminates these time derivatives using the leading-order approximation for $\partial_t \boldsymbol{u}$.

For the equations that yield explicit ODE systems under spatial discretization, in other words everything except the original implicit PSM equation, a dedicated ODE integrator like VODPK offered about 20% better performance than the DAE integrator in the second set of experiments with random initial conditions. This is because the timestep is controlled primarily by accuracy constraints on the leading-order advection term, rather than by the stability of the diffusive terms.

10. Conclusion

PSM derived equation (1.6) as an improved description of the evolution of the vertically averaged horizontal velocity in a thin liquid-metal layer permeated by an imposed vertical magnetic field. PSM's equation improves the earlier equation (1.1) derived by Sommeria & Moreau (1982) by including inertial corrections to the flow in the Hartmann layers. These corrections appear as cubically nonlinear terms in addition to the leading-order linear drag exerted by the Hartmann layers on the core fluid. When written in terms of a streamfunction and vorticity as in (1.8), we recognize many of the nonlinear terms in the PSM equation as being identical to terms appearing in the anticipated vorticity and anticipated velocity methods. In particular, the $[\psi, [\psi, \omega]]$ term from the anticipated vorticity method that is responsible for anisotropic diffusion of vorticity along streamlines is common to all three equations. This is the only extra term involving second derivatives of the vorticity, so it dominates the behaviour at high wavenumbers as seen in the evolution of the enstrophy and palinstrophy.

In the original PSM equation, the nonlinear diffusion of vorticity along streamlines is suppressed at high wavenumbers by the $\partial_t [\psi, \omega]$ term that contains mixed spatio-temporal derivatives (Benjamin *et al.* 1972). This causes the decay rate of short-wave perturbations to saturate at a finite value, as shown in figure 2, rather than growing indefinitely in proportion to the wavenumber squared. The implicit property of the PSM equation offers no serious obstacle to obtaining numerical solutions via the formulation as a differential-algebraic system presented above. The numerical solutions have been verified by recovering the correct phase speeds and decay rates of linear waves, and by comparison with solutions obtained independently from the small Mach number limit of the compressible anticipated velocity method using a lattice Boltzmann formulation (Dellar 2004). However, for realistic parameter values the implicit terms only become significant at extremely high horizontal wavenumbers, with $k\ell = O(NHa/\delta) \gg 1$ for a domain of width ℓ. These are far beyond the validity of the shallow-layer approximation, so we may replace the original PSM equation by the fully explicit equation given in (2.13). This equation was derived by eliminating the time derivatives in $\partial_t [\psi, \omega]$ using the leading-order approximation $\partial_t \omega + [\psi, \omega] = \kappa(\omega_0 - \omega)$. This explicit equation is much less computationally expensive than the original PSM equation, and provides virtually indistinguishable results for the parameter values relevant to laboratory experiments, and in the numerical experiments presented above.

The numerical experiments suggest that the qualitative behaviour of the PSM equation, in either implicit or explicit form, is much closer to the anticipated velocity method (Benzi *et al.* 1990, 1992; Dellar 2004) than the anticipated vorticity method. The PSM equation and the anticipated velocity method both contain the additional nonlinear terms $[\psi_y, \omega\psi_x]$ and $[\omega\psi_y, \psi_x]$. These terms lead to additional dissipation of energy, even without viscosity, as calculated in §5. Although there is no simple expression for the energy dissipation rate in either the implicit or explicit forms of the PSM equation, we derived upper and lower bounds for the energy dissipation rate under the explicit PSM equation in §5. The $[\psi_y, \omega\psi_x]$ and $[\omega\psi_y, \psi_x]$ terms are also responsible for spreading vortex patches, and represent the effects of Ekman pumping in the Hartmann layers on the vertically averaged flow. In a coherent vortex, Ekman pumping causes an enhanced radial inflow of fluid in the Hartmann layers. Incompressibility therefore requires a compensating outflow within the core. The leading-order horizontal velocity, and thus the vertical vorticity $\omega_z = \partial_x u_y - \partial_y u_x$, are both larger in the core than in the Hartmann layers (see figure 1), so the Ekman

pumping drives a net outward transport of vorticity, despite there being no radial component to the vertically averaged horizontal velocity.

From the same realization of random initial conditions, the PSM equation and the anticipated velocity method both develop flows that look far more "self-organized" than either the Navier–Stokes equations or the anticipated vorticity method at the same time, as shown in figures 6 and 7. In particular, large and nearly axisymmetric vortices form much more readily in the PSM and anticipated velocity equations. The tendency towards axisymmetry is accelerated by the $[\psi, [\psi, \omega]]$ term that diffuses vorticity along streamlines, while the $[\psi_y, \omega\psi_x]$ and $[\omega\psi_y, \psi_x]$ terms cause outward expansion of curved streamlines. The parameters used in the numerical experiments are reasonably representative of laboratory experiments, although both dimensionless diffusivities β and ν are about ten times too large, and ν is perhaps relatively small compared with β. It therefore seems plausible that the self-organization into large coherent vortices seen by Sommeria (1986, 1988), or the merging of many small vortices created by a Kelvin–Helmholtz instability into a few large vortices seen by Alboussière *et al.* (1999), may be attributed at least partially to the additional effects described by the PSM equation, and not entirely to the self-organizing behaviour of the pure two-dimensional Navier–Stokes equations. The vortex merging seen by Messadek & Moreau (2002) may also be due to the same mechanism, although the Hartmann layers in their experiments were almost certainly turbulent, and thus not described by the PSM equation.

The numerical experiments were conducted in a doubly periodic domain for simplicity, but the approach used could be extended to finite domains. It is perhaps easiest to retain the streamfunction–vorticity formulation, and impose two boundary conditions on the streamfunction ψ and its normal derivative $\boldsymbol{n} \cdot \nabla\psi$. Alternatively, the incompressible Navier–Stokes equations in velocity–pressure form may be formulated as a system of differential-algebraic equations (DAEs) using the Galerkin finite element method. Incompressibility is enforced by a series of algebraic constraints (Gresho & Sani 2000). This formulation should extend easily to include the extra spatio-temporal derivatives of the velocity appearing in equation (1.6). The omitted forcing and drag terms would also be easy to incorporate.

Finally, the formation of vortex patches is reminiscent of the Prandtl–Batchelor theorem (Batchelor 1956) predicting the homogenization of vorticity inside regions of closed streamlines for steady flows in the large Reynolds number limit. Although the theorem strictly applies only to steady flows, it is found to give a good description of some unsteady flows such as the von Kármán vortex street created in flow past a circular cylinder (Davidson 2001; Matsuura & Yamagata 1985). The vortices in the street behind the cylinder are found to be made up of patches of nearly uniform vorticity, even though the flow is unsteady. In a geophysical context, Rhines & Young (1982) predicted the formation of constant-potential-vorticity patches in unsteady rotating flows, provided either the time-averaged streamlines or the mean potential vorticity isolines are closed. The qualitative behaviour of solutions of the PSM equation, with the large patches of almost uniform vorticity seen in figures 5 and 7, is thus similar to what one might expect from the long-time and nearly inviscid limit of the two-dimensional Navier–Stokes equations, but the tendency towards homogenization of vorticity is caused by Ekman pumping in the boundary layers, rather than directly by horizontal viscous diffusion. It would be interesting to extend the numerical solutions to include the algebraic forcing and drag terms, and compare the outcome with the modified Prandtl–Batchelor theorem obtained by Yamagata & Matsuura (1981) that includes dissipation through both drag and viscosity, and with

the laboratory experiments of Frank *et al.* (2001) for quasi-two-dimensional MHD flow past a cylinder.

REFERENCES

ALBOUSSIÈRE, T., USPENSKI, V. & MOREAU, R. 1999 Quasi-2D MHD turbulent shear layers. *Expl Therm. Fluid Sci.* **20**, 19–24.

ALEMANY, A., MOREAU, R., SULEM, P. L. & FRISCH, U. 1979 Influence of an external magnetic field on homogeneous MHD turbulence. *J. Méc,* **18**, 277–313.

BASDEVANT, C. & SADOURNY, R. 1983 Parametrization of virtual scale in numerical-simulation of two-dimensional turbulent flows. *J. Mech. Theor. Appl.* special issue, 243–269.

BATCHELOR, G. K. 1956 Steady laminar flow with closed streamlines at large Reynolds numbers. *J. Fluid Mech.* **1**, 177–190.

BATCHELOR, G. K. 1969 Computation of the energy spectrum in homogeneous two-dimensional turbulence. *Phys. Fluids suppl.* II **12**, 233–239.

BENJAMIN, T. B., BONA, J. L. & MAHONY, J. J. 1972 Model equations for long waves in nonlinear dispersive systems. *Phil. Trans. R. Soc. Lond.* A **272**, 47–78.

BENZI, R., SUCCI, S. & VERGASSOLA, M. 1990 Turbulence modelling by nonhydrodynamic variables. *Europhys. Lett.* **13**, 727–732.

BENZI, R., SUCCI, S. & VERGASSOLA, M. 1992 The lattice Boltzmann equation: theory and applications. *Phys. Rep.* **222**, 145–197.

BRENAN, K. E., CAMPBELL, S. L. & PETZOLD, L. R. 1995 *Solution of Initial-Value Problems in Differential-Algebraic Equations*. Philadelphia: SIAM.

BRETHERTON, F. P. & HAIDVOGEL, D. B. 1976 Two-dimensional turbulence above topography. *J. Fluid Mech.* **78**, 129–154.

BROWN, P. N., BYRNE, G. D. & HINDMARSH, A. C. 1989 VODE, a variable-coefficient ODE solver. *SIAM J. Sci. Statist. Comput.* **10**, 1038–1051.

BROWN, P. N., HINDMARSH, A. C. & PETZOLD, L. R. 1994 Using Krylov methods in the solution of large-scale differential-algebraic systems. *SIAM J. Sci. Comput.* **15**, 1467–1488.

BROWN, P. N., HINDMARSH, A. C. & PETZOLD, L. R. 1998 Initial condition calculation for differential-algebraic systems. *SIAM J. Sci. Comput.* **19**, 1495–1512.

BÜHLER, L. 1996 Instabilities in quasi-two-dimensional magnetohydrodynamic flows. *J. Fluid Mech.* **326**, 125.

CAMASSA, R., HOLM, D. D. & LEVERMORE, C. D. 1996 Long-time effects of bottom topography in shallow water. *Physica* D **98**, 258–286.

CHEN, S. & DOOLEN, G. D. 1998 Lattice Boltzmann method for fluid flows. *Annu. Rev. Fluid Mech.* **30**, 329–364.

DAVIDSON, P. A. 1995 Magnetic damping of jets and vortices. *J. Fluid Mech.* **299**, 153–186.

DAVIDSON, P. A. 2001 *An Introduction to Magnetohydrodynamics*. Cambridge University Press.

DELLAR, P. J. 2003 Dispersive shallow water magnetohydrodynamics. *Phys. Plasmas* **10**, 581–590.

DELLAR, P. J. 2004 An anticipated velocity lattice Boltzmann method for two dimensional turbulence. *J. Statist. Phys.* (submitted).

FRANK, M., BARLEON, L. & MULLER, U. 2001 Visual analysis of two-dimensional magneto-hydrodynamics. *Phys. Fluids* **13**, 2287–2295.

FRIGO, M. & JOHNSON, S. G. 1998 FFTW: An adaptive software architecture for the FFT. In *Proc. IEEE Intl Conf. on Acoustics, Speech, and Signal Processing, Seattle, 1998*, vol. 3, pp. 1381–1384. Piscataway, NJ: IEEE Press (available from http://www.fftw.org/).

FRISCH, U. 1995 *Turbulence: The Legacy of A. N. Kolmogorov*. Cambridge University Press.

GEURTS, B. J. & HOLM, D. D. 2003 Regularization modeling for large-eddy simulation. *Phys. Fluids* **15**, L13–L16.

GILMAN, P. 2000 Magnetohydrodynamic "shallow water" equations for the solar tachocline. *Astrophys. J. Lett.* **544**, 79–82.

GOLUB, G. H. & VAN LOAN, C. F. 1996 *Matrix Computations*, 3rd edn. Johns Hopkins University Press.

GREEN, A. E. & NAGHDI, P. M. 1976 A derivation of equations for wave propagation in water of variable depth. *J. Fluid Mech.* **78**, 237–246.

GRESHO, P. M. & SANI, R. L. 2000 *Incompressible Flow and the Finite Element Method, Volume 2, Isothermal Laminar Flow*. Wiley.

HOLLOWAY, G. 1992 Representing topographic stress for large-scale ocean models. *J. Phys. Oceanogr.* **22**, 1033–1046.

KELLAY, H. & GOLDBURG, W. I. 2002 Two-dimensional turbulence: a review of some recent experiments. *Rep. Prog. Phys.* **65**, 845–894.

KIDA, S., YAMADA, M. & OHKITANI, K. 1988 The energy-spectrum in the universal range of two-dimensional turbulence. *Fluid Dyn. Res.* **4**, 271–301.

KOLESNIKOV, Y. B. & TSINOBER, A. B. 1974 Experimental investigation of two-dimensional turbulence behind a grid. *Izv. Akad. Nauk SSSR, Meh. Zidk. Gaza* (No. 4), 146–150 (in Russian).

KRAICHNAN, R. H. 1967 Inertial ranges in two-dimensional turbulence. *Phys. Fluids* **10**, 1417–1423.

KRAICHNAN, R. H. & MONTGOMERY, D. 1980 Two-dimensional turbulence. *Rep. Prog. Phys.* **43**, 547–619.

LERAY, J. 1934 Sur les movements d'un fluide visqueux remplaissant l'espace. *Acta Math.* **63**, 193–248, in French. (Available in an English translation "On the motion of a viscous liquid filling space" by R. E. Terrel at http://www.math.cornell.edu/~bterrell/leray.shtml.)

MATSUURA, T. & YAMAGATA, T. 1985 A numerical study of a viscous flow past a circular cylinder on an f-plane. *J. Met. Soc. Japan* **63**, 151–167.

MATTHAEUS, W. H. & MONTGOMERY, D. 1980 Selective decay hypothesis at high mechanical and magnetic Reynolds numbers. *Ann. New York Acad. Sci.* **357**, 203–222.

MCWILLIAMS, J. C. 1984 The emergence of isolated coherent vortices in turbulent flow. *J. Fluid Mech.* **146**, 21–43.

MESSADEK, K. & MOREAU, R. 2002 An experimental investigation of MHD quasi-two-dimensional turbulent shear flows. *J. Fluid Mech.* **456**, 137–159.

MILES, J. & SALMON, R. 1985 Weakly dispersive nonlinear gravity waves. *J. Fluid Mech.* **157**, 519–531.

MILLER, J., WEICHMAN, P. B. & CROSS, M. C. 1992 Statistical mechanics, Euler's equation, and Jupiter's Red Spot. *Phys. Rev.* A **45**, 2328–2359.

MINION, M. L. & BROWN, D. L. 1997 Performance of under-resolved two-dimensional incompressible flow simulations, II. *J. Comput. Phys.* **138**, 734–765.

MOREAU, R. 1990 *Magnetohydrodynamics*. Kluwer.

MOREAU, R. 1998 MHD turbulence at the laboratory scale: Established ideas and new challenges. *Appl. Sci. Res.* **58**, 131–147.

PETZOLD, L. R. 1983 A description of DASSL: a differential/algebraic system solver. In *Scientific Computing* (ed. R. S. Stepleman *et al.*), pp. 65–68. North-Holland.

POLVANI, L. M., MCWILLIAMS, J. C., SPALL, M. A. & FORD, R. 1994 The coherent structures of shallow-water turbulence: Deformation-radius effects, cyclone/anticyclone asymmetry and gravity-wave generation. *Chaos* **4**, 177–186.

POTHÉRAT, A., SOMMERIA, J. & MOREAU, R. 2000 An effective two-dimensional model for MHD flows with transverse magnetic field. *J. Fluid Mech.* **424**, 75–100 (referred to herein as PSM).

RHINES, P. B. 1979 Geostrophic turbulence. *Annu. Rev. Fluid. Mech.* **11**, 401–441.

RHINES, P. B. & YOUNG, W. R. 1982 Homogenization of potential vorticity in planetary gyres. *J. Fluid Mech.* **122**, 347–367.

ROBERT, R. & SOMMERIA, J. 1991 Statistical equilibrium states for 2-dimensional flows. *J. Fluid Mech.* **229**, 291–310.

ROBERTS, P. H. 1967 *An Introduction to Magnetohydrodynamics*. Longmans.

SAAD, Y. 1996 *Iterative Methods for Sparse Linear Systems*. Boston: PWS (available from http://www-users.cs.umn.edu/~saad/books.html). Second edition (2003) published by SIAM, Philadelphia.

SAAD, Y. & SCHULTZ, M. H. 1985 GMRES – a generalized minimal residual algorithm for solving nonsymmetric linear systems. *SIAM J. Sci. Statist. Comput.* **7**, 856–869.

SADOURNY, R. & BASDEVANT, C. 1981 A class of operators suitable for modeling turbulent-diffusion in dimension 2. *C. R. Acad. Sci. Paris* II **292**, 1061–1064 (in French).

SADOURNY, R. & BASDEVANT, C. 1985 Parameterization of subgrid scale barotropic and baroclinic eddies in quasi-geostrophic models – anticipated potential vorticity method. *J. Atmos. Sci.* **42**, 1353–1363.

SALMON, R. 1998 *Lectures on Geophysical Fluid Dynamics*. Oxford University Press.

SHERCLIFF, J. A. 1965 *A Textbook of Magnetohydrodynamics*. Pergamon.

SOMMERIA, J. 1986 Experimental study of the two-dimensional inverse energy cascade in a square box. *J. Fluid Mech.* **170**, 139–68.

SOMMERIA, J. 1988 Electrically driven vortices in a strong magnetic field. *J. Fluid Mech.* **189**, 553–569.

SOMMERIA, J. & MOREAU, R. 1982 Why, how, and when, MHD turbulence becomes two-dimensional. *J. Fluid Mech.* **118**, 507–518.

SUCCI, S. 2001 *The Lattice Boltzmann Equation: For Fluid Dynamics and Beyond*. Oxford University Press.

TABELING, P. 2002 Two-dimensional turbulence: a physicist approach. *Phys. Rep.* **362**, 1–62.

TING, A. C., MATTHAEUS, W. H. & MONTGOMERY, D. 1986 Turbulent relaxation processes in magnetohydrodynamics. *Phys. Fluids* **29**, 3261–3274.

TREFETHEN, L. N. & BAU, D. 1997 *Numerical Linear Algebra*. Philadelphia: SIAM.

VALLIS, G. K. & HUA, B.-L. 1988 Eddy viscosity of the anticipated potential vorticity method. *J. Atmos. Sci.* **45**, 617–627.

VERRON, J. & SOMMERIA, J. 1987 Numerical simulation of a two-dimensional turbulence experiment in magnetohydrodynamics. *Phys. Fluids* **30**, 732–739.

WEISS, J. B. & MCWILLIAMS, J. C. 1993 Temporal scaling behavior of decaying two-dimensional turbulence. *Phys Fluids* A **5**, 608–621.

YAMAGATA, T. & MATSUURA, T. 1981 A generalization of Prandtl–Batchelor theorem for planetary fluid flows in a closed geostrophic contour. *J. Met. Soc. Japan* **59**, 615–619.